Review on Pore Structure Characterization and Microscopic Flow Mechanism of CO 2 Flooding in Porous Media

Citation: Tang, Yong, Hou, Chengxi, He, Youwei, Wang, Yong, Chen, Yulin et al. 2020. "Review on Pore Structure Characterization and Microscopic Flow Mechanism of CO 2 Flooding in Porous Media." Energy Technology, 9 (1).

As Published: http://dx.doi.org/10.1002/ente.202000787

Publisher: Wiley

Persistent URL: https://hdl.handle.net/1721.1/140613

Version: Author's final manuscript: final author's manuscript post peer review, without publisher's formatting or copy editing

Review on pore structure characterization and microscopic flow mechanism of CO_2 flooding in porous media

Yong Tang[1], Chengxi Hou[1], Youwei He[1,]*, Yong Wang[1], Yulin Chen[1], Zhenhua Rui[2,]*

[1] State Key Laboratory of Oil and Gas Reservoir Geology and Exploitation, Southwest Petroleum University, Chengdu 610500, China.

[2] Massachusetts Institute of Technology, Cambridge, MA 02139, USA.

*Correspondence should be addressed to youweihe_cupb@163.com and zrui@mit.edu.

ABSTRACT

Understanding of pore structure and microscopic flow mechanism at pore-scale is significant for enhancing oil recovery by CO_2 flooding. This paper analyzes and compares the pore structure characterization and the microscopic flow mechanism of CO_2 flooding. The pore structure can be captured using experimental analysis, image analysis, and digital core technique. Digital core approach shows broad application for pore structure characterization since it is reusable and visible. Pore-scale flow can be directly observed using visual models, however the pressure and temperature that visual models can withstand need to be improved. X-ray CT and NMR are preferred to be used to monitor the fluid transport and distribution during CO_2 displacement in actual cores. The flow in porous media can be also modeled by Molecular Dynamics (MD) and Lattice Boltzmann Method (LBM). LBM is efficient in simulating multi-phase fluid flow in porous media, and exhibits promising application in CO_2 flooding in tight oil reservoirs since it achieves the parallel computing and can deal with complex boundaries. This paper presents detailed analysis for pore structure characterization and microscopic flow mechanism of CO_2 flooding in porous media, which can further help to design and optimize CO_2 flooding schemes to improve oil recovery.

Keywords:

CO_2 flooding; Pore structure; Microscopic flow mechanism; Porous media; Enhanced oil recovery.

1. Introduction

Rapidly rising emissions of greenhouse gases into the atmosphere lead to the greenhouse effect and accelerate the exacerbation of global climate.[1] Greenhouse gases include carbon dioxide (CO_2), ozone (O_3), nitric oxide (N_2O), methane (CH_4), hydrogen fluoride, chlorine carbide class (CFCs, HFCs, HCFCs), perfluorinated carbide (PFCs) and sulfur hexafluoride (SF_6), etc. The concentration of CO_2 is the highest in the atmosphere among greenhouse gases, and it significantly dominates global warming than any other greenhouse gases.[2] The process of the greenhouse effect and the impact of greenhouse gases on global warming are shown in **Figure 1**.

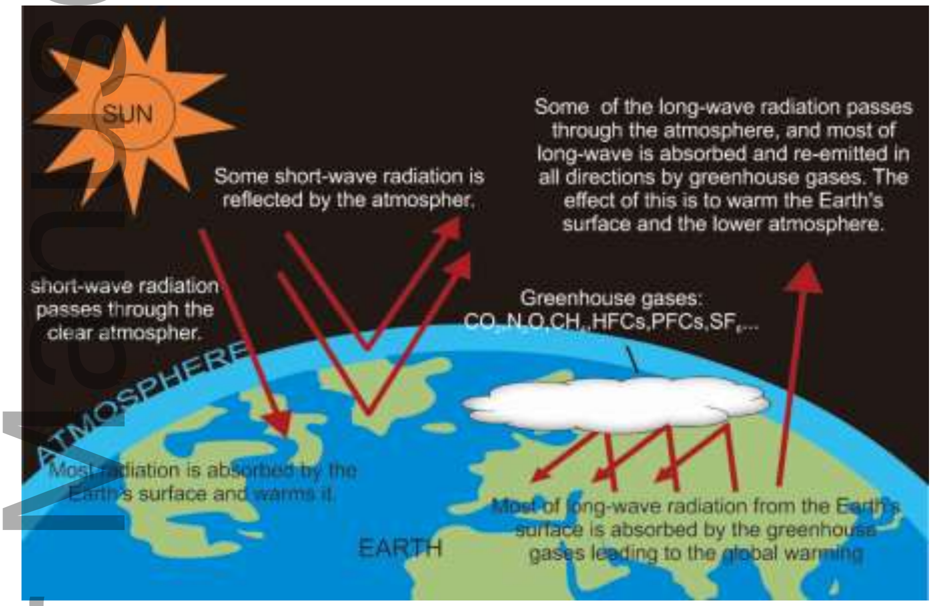

Figure 1. The schematic of greenhouse effect.

Carbon is one of the most important elements of earth's structure and living things. It widely exists in the biosphere, lithosphere, hydrosphere and atmosphere, and circulates continuously with the movement of the Earth. CO_2 plays an important role in the cycle. Green plants absorb CO_2 from the atmosphere, and CO_2 is converted into organic matter and oxygen is also released through photosynthesis with the participation of water, shown in **Figure 2**.[3],[4] Before the industrial revolution, the carbon cycle has been kept in balance for millions of years. After the industrial revolution, human beings began to utilize fossil fuels to obtain energy. The balance of nature is thus destroyed, leading to climate anomalies (e.g., global warming) due to the increased concentration of CO_2 caused by the burning of fossil fuels and other industrial activities. Therefore, reducing emissions of CO_2 and other greenhouse gases is essential for protecting the natural environment.[5],[6]

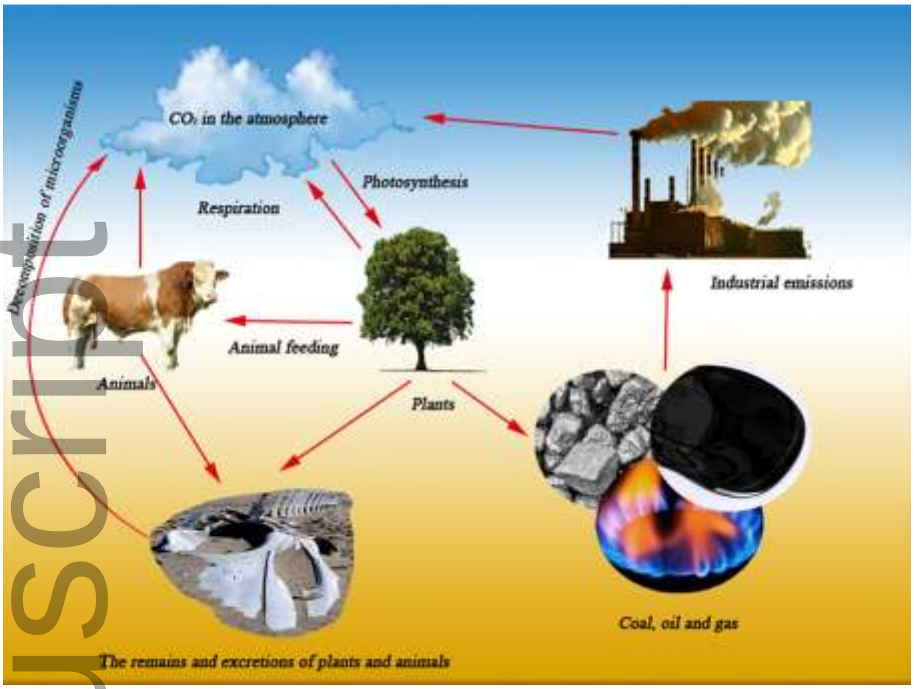

Figure 2. The schematic of global carbon cycle.

At present, carbon emissions can be reduced by decreasing energy consumption, improving energy utilization efficiency, replacing fossil fuels with clean energy (e.g., solar energy, wind energy, geothermal energy, hydrogen energy), carbon capture and storage (CCS). However, most of the clean energy are still hard to completely replace fossil fuels in the near future due to the safety, technology availability and economical efficiency.[7] CCS is an important technological means to reduce carbon emission.[8],[9] However, CCS requires high costs and may cause leakage of carbon since the captured carbon is usually sequestrated in saline aquifer, coal seams, depleted reservoirs, etc.[10]-[12] Therefore, Carbon Capture, Utilization and Storage (CCUS) has been acknowledged as a promising technology to achieve efficient reduction of carbon and also generate economic benefits, which is more practical and economical.[13]

CO_2 is an important materials for industry and has been applied in many fields as shown in **Figure 3**.[14],[15] In the food industry, CO_2 is used in the production of carbonized beverages, food preservation, and industrial processing as refrigerant and protective gas. It can be also applied to synthesize chemicals, drugs, polymers, etc., such as degradable plastics. High purity CO_2 is mainly used in medical research and clinical diagnosis, such as carbon dioxide laser, calibration gas of detection instrument and preparation of other special mixture. Supercritical CO_2 ($scCO_2$) can be considered as a solvent to dissolve nonpolar, nonionic and low molecular weight compounds. $scCO_2$ can be also used to exploit geothermal energy since it is effective in heat transfer and flow.[16]-[18] CO_2 also attracts broad interests in the oil industry to enhance hydrocarbon recovery and also achieve the geological storage of CO_2, including CO_2 flooding, CO_2 huff-n-puff, $scCO_2$ fracturing, and replacement exploitation of gas hydrate[20]-[29] etc.

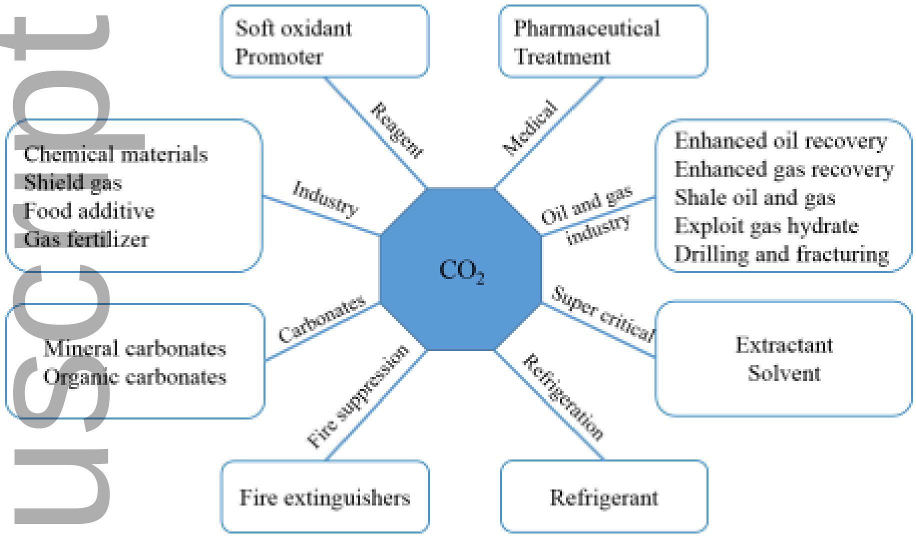

Figure 3. CO_2 utilization in various industries (modified from Gulzar et al. [30]).

However, the mechanism of CO_2 enhanced hydrocarbon recovery at pore-scale is still unclear. The impact of pore structure on displacement efficiency and displacement process during CO_2 flooding at pore-scale are significant and need to be discussed in detail. More attention needs to be paid to pore structure characterization and flow mechanism during CO_2 flooding in porous media.

2. Pore structure characterization

The pore structure in rocks refers to the type, size, distribution and interconnection of pores and throat in stone. The pore structure in rocks is composed of pore and throat. The pore is the enlarged part of the system, and the small part connecting the pore is called the throat. Pore is the basic storage space of fluid in rocks, and throat is the important channel of fluid.[31]-[33] The pores reflect the storage capacity of rocks, and the size, shape and connectivity of the throat determine the rock permeability.[34]

Various techniques and methods have been developed to describe the pores and throat in rock, including experimental analysis, image analysis and digital core technique.

2.1. Experimental analysis

The experimental methods are mainly composed of mercury intrusion porosimetry (MIP) (i.e., constant rate MIP and high-pressure MIP), nuclear magnetic resonance (NMR), and gas adsorption.

Generally, experimental methods can quantitatively characterize pore and throat by the measurement of fluids parameters in the porous media. **Table 1** illustrates the difference among experimental methods.

Table 1. Details on the various experiments of pore structure characterization

Techniques	Measurement range	Method of measurement	Parameters	References
Constant rate MIP	≥ 0.12 μm	Mercury injection pressure and volume are used to characterize pore structure	Capillary pressure, pore radius, pore volume, porosity, specific surface	[35],[36]
High pressure MIP	1.8 nm - 180 μm			
NMR	0.1 nm – 10 mm	The pore structure is inverted based on relaxation time of fluids in pore	T2 relaxation time of pore fluid, pore size distribution, fluid distribution, porosity	[37]
Gas adsorption	0.3 nm - 200 μm	The pore structure is characterized by the conversion of adsorbed gas volume	Pore size distribution, specific surface, porosity, pore volume	[38]

2.1.1. Mercury intrusion porosimetry

Typically, mercury is a non-wetting liquid and has a high surface tension when in contact with other materials. The structures of pore and throat is considered as a series of irregular capillary network for MIP, and mercury is injected into the network by an external force. The capillary pressure that forces mercury into the pores is directly related to the size of pore and throat, generally lower pressure required for macro-pores and higher pressure needed for micro-pores. The relationship between capillary pressure and pore radius can be described by **Equation (1)**.

$$P_c = \frac{2\sigma \cos\theta}{r} \tag{1}$$

where P_c is the capillary pressure, and r means the pore radius. σ is the surface tension, and θ represents the contact angle.[39],[40]

In MIP test, the injected medium is mercury, and the displaced medium is air. The surface tension between mercury and air is 485 mN/m, and the wetting angle is 140°.[41] Therefore, the pore radius distribution can be actually obtained by measuring capillary pressure in MIP test. Typical capillary pressure curves of tight sandstone during MIP test are shown in **Figure 4**. Mercury injection curve (Curve I) displays the process of mercury injecting into the porous media. With the increase of pressure, mercury begins to enter the pore and throat of the porous media. The pressure rises rapidly due to the few macropores and throats. Capillary pressure increases with the increase of mercury injection volume in Curve I. When the maximum injection pressure is reached, the injection pressure is reduced gradually and mercury flows out of the porous media (Curve II). Several parameters related to the pore structure can be observed from the curves. P_d is the capillary pressure at which mercury begins to enter the porous media, corresponding to the maximum pore throat radius. P_{50} represents the capillary pressure at mercury saturation of 50%, which increases with the decrease of permeability of the porous media. $S_{\max}$ means the volume factor of mercury in the porous media at the highest injection pressure, which will become smaller for more immeasurable micropores.

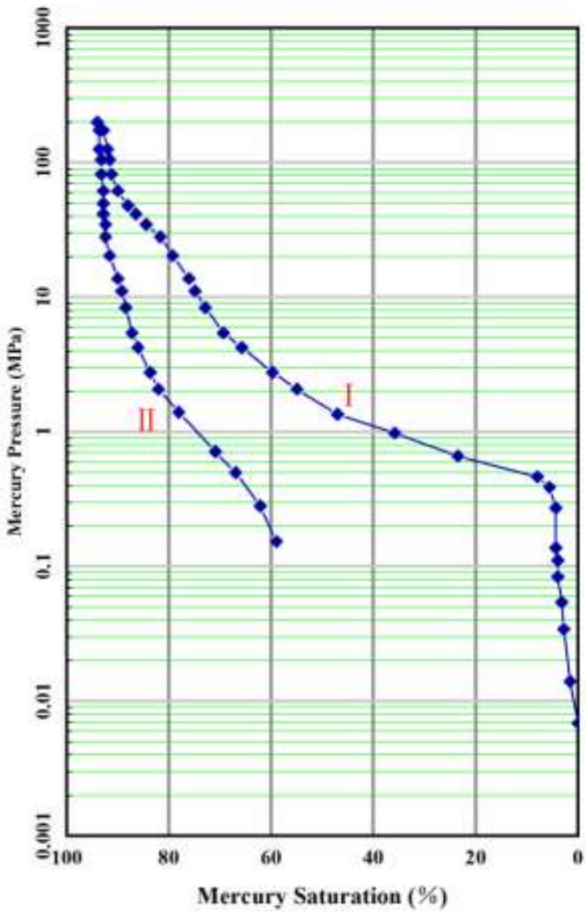

Figure 4. Typical capillary curve of the tight sandstone.

Two types of MIP are usually used to quantitatively characterize pore structure, including high pressure MIP and constant rate MIP.

It achieves wider measurement range of pore and throat structure (e.g., radius, distribution, volumes) through High pressure MIP due to higher mercury injection pressure. However, high pressure may generate artificial cracks in the core, and cause information loss in the measurement of macropores. The highest injection pressure is about 400 MPa, corresponding to a pore radius of about 1.8 nm.

Mercury is injected into the porous media at a very low rate, which ensures the pseudo-steady injection of mercury during constant rate MIP. Differences of pore structure directly affect the two-phase interface between mercury and air., resulting in changes of the capillary pressure. Hence, the pore structure characteristics of the rock can be inferred from the mercury injection pressure curve. **Figure 5** shows the process of constant rate MIP.[42] Firstly, mercury enters the Throat I due to pressure difference. Then, mercury breaks through Throat I and enters Pore 1 with the increase of pressure, while the pressure decreases at the same time. Thirdly, mercury fills up pore 1 and enters Throat II gradually, leading to the increase of pressure. Until the breakthrough pressure is reached, mercury enters Pore 3 and the pressure decreases further. After both the pores no smaller than Throat I and pores connected to Throat I are filled up, mercury begins to enter the pore controlled by smaller throats. The process is repeated until the pressure reaches the upper limit of the constant rate MIP. The throat radius is determined by the mercury breakthrough pressure, and the pore volume is measured by the injected mercury volume. Constant rate MIP can identify the throat so that the radius of throat and pore can be measured respectively, while conventional MIP are unable to distinguish throat from pore and throat.[43] The parameters of pore and throat can be accurately obtained by constant rate MIP, however the minimum pore radius that can be tested is only 0.12 μm due to the limit of injection pressure.[44] Furthermore, it usually takes a long time since the injection rate is quite low and kept constant.

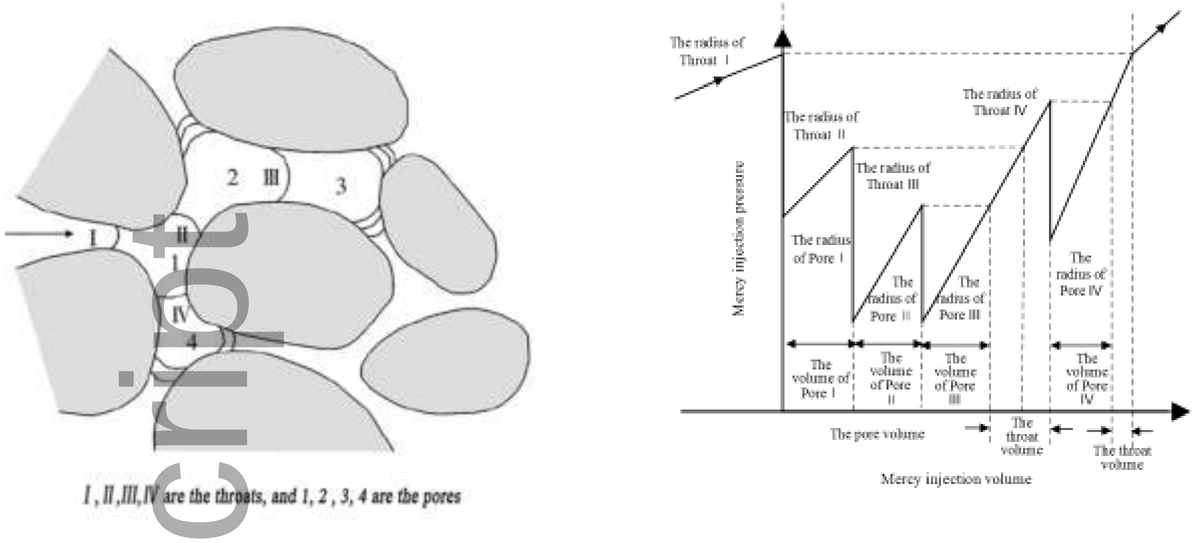

(a) (b)

Figure 5. Introduction of constant rate MIP. (a) The route of mercury in the core; (b) Pressure change during injection process.[42]

MIP can determine the pore structure characteristics according to the capillary pressure curve of mercury injected into the porous media. MIP is one of the commonly used methods for quantitative evaluation of pore structure attributed to its simple testing process and low cost. However, it is hard to determine microscopic structures of nano-scale pore and throat by MIP due to the limitation of mercury injection pressure.

2.1.2. Nuclear Magnetic Resonance

The pore structure characteristic and fluid distribution can be determined using NMR by testing the nuclear magnetic signal of hydrogen-containing fluids in a porous media.[45] The process of NMR can be found in **Figure 6**. The spinning motion of a charged nucleus creates a magnetic moment. In general, the nuclear magnetic moment of nucleus system is disordered and shows no magnetism at macro level (**Figure 6** a). The nuclear magnetic moment in a static magnetic field will gradually change into the same direction as the static magnetic field (**Figure 6** b, c). At this point, most of the nucleus are in a low energy state and a few are in a high energy state. If a strong pulsed magnetic field at Larmor frequency is applied at the perpendicular direction of the static magnetic field after the nuclear magnetic moment reaching equilibrium, the lower state nucleus will absorb the energy of the pulsed magnetic field and gradually transit to the higher energy state.[46] And the nuclear magnetic moment will rotate in the direction of pulsed magnetic field (**Figure 6** d). After the pulsed magnetic field is removed, the nuclear magnetic moment precesses in the direction of static magnetic field (**Figure 6** e). Finally, the nuclear magnetic moment returns to the equilibrium state (**Figure 6** f).

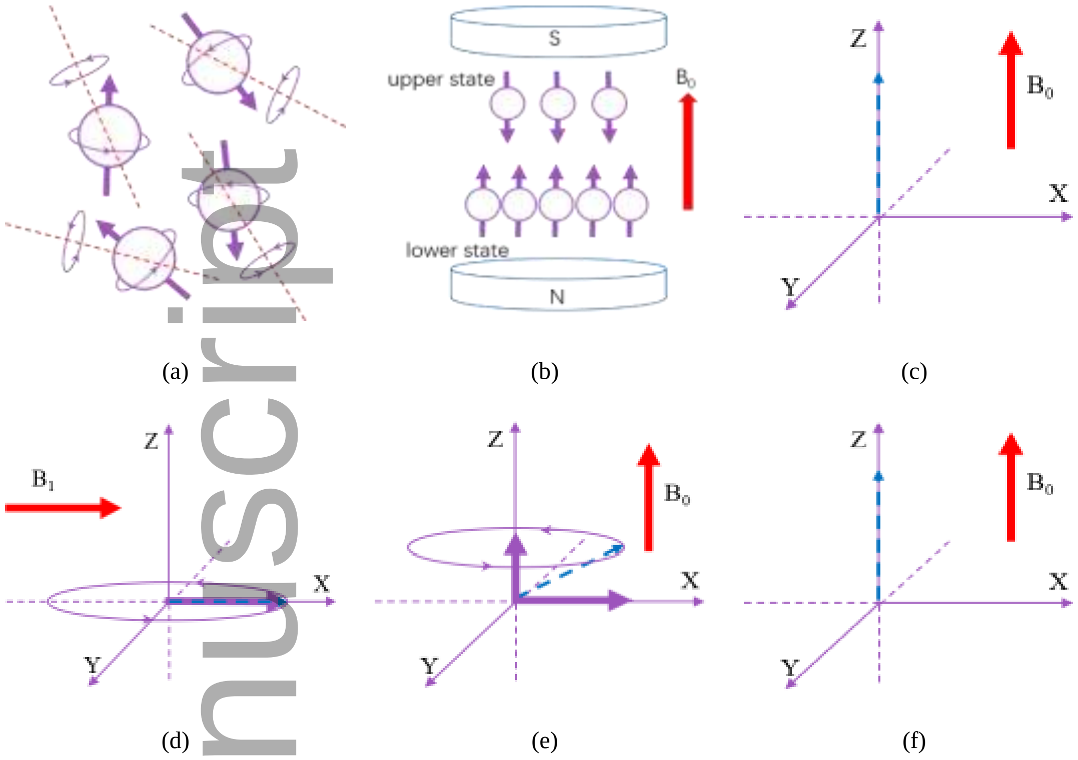

(a) (b) (c)

(d) (e) (f)

Figure 6. Schematic diagram of the NMR process. (a) Spin nucleus in disordered state; (b) The magnetic moments of nucleus under a static magnetic field; (c) The macroscopic magnetic moment of nucleus is in the same direction as the static magnetic field; (d) The nuclear magnetic moment rotates under transverse pulsed magnetic field; (e) The nuclear magnetic moment precesses after the pulsed magnetic field is removed; (f) The nuclear magnetic moment returns to equilibrium state.

The longitudinal relaxation times (T_1) and transverse relaxation times (T_2) are commonly measured using NMR. After the pulsed magnetic field is removed, the nucleus in high energy state release energy and transit into low energy state, and the vector component of nuclear magnetic moment in the direction of static magnetic field increases to the initial value gradually. Meanwhile, the spin of the nucleus causes phase dispersion, and vector component of nuclear magnetic moment in the direction of pulsed magnetic field decreases to 0 rapidly. T_1 and T_2 refer to the characteristic time for the vector component of nuclear magnetic moment returning to the equilibrium state in the direction of static magnetic field and pulsed magnetic field respectively. T_1 is usually ignored during experimental tests. It is preferred to monitor T_2 in the laboratory measurement since it can be obtained much faster. T_2 can be calculated by three relaxation mechanisms with **Equation (2)**.[47]-[49]

$$\frac{1}{T_2}=\frac{1}{T_{2B}}+\frac{1}{T_{2D}}+\frac{1}{T_{2S}} \qquad (2)$$

where T_2 is the transverse relaxation time. T_{2B}, T_{2D}, and T_{2S} are the bulk relaxation time, diffusion-induced relaxation time, and surface relaxation time, respectively.[50],[51]

Generally, T_{2B} and T_{2D} are much longer than T_2 and T_{2S}, hence $\frac{1}{T_{2B}}$ and $\frac{1}{T_{2D}}$ can be ignored in the measurement. Therefore, T_2 is directly related to T_{2S} (**Equation (3)**).[52]-[54]

$$\frac{1}{T_2} = \frac{1}{T_{2S}} = \rho_c \frac{S}{V} \tag{3}$$

where ρ_c is the surface relaxation coefficient, S means the pore surface, and V denotes the pore volume.

The pore radius can be calculated by **Equation (4)**[55],[56] .

$$r = \frac{F_r}{(S/V)} = \rho_c F_r T_2 \tag{4}$$

where F_r is the dimensionless pore shape factor, and r is the pore radius.

F_r and ρ_c are constant for the same porous media. Therefore, the pore size distribution can be directly calculated by T_2 spectrum when ρ_c and F_r are determined.

NMR can detect the nuclear magnetic signals of fluids in porous media. **Figure 7** shows typical T_2 spectrum of five sandstone cores filled with pure water among all 264 samples.[57] Bimodal distribution can be observed for most T_2 spectrum of sandstone (Patterns A, B, and E), which is the same as the pore radius distribution. Unimodel distribution (Pattern C) means that the core sample is homogeneous in pore and throat. Triple-peak distribution (Pattern D) implies that there may be microfractures in the core sample.

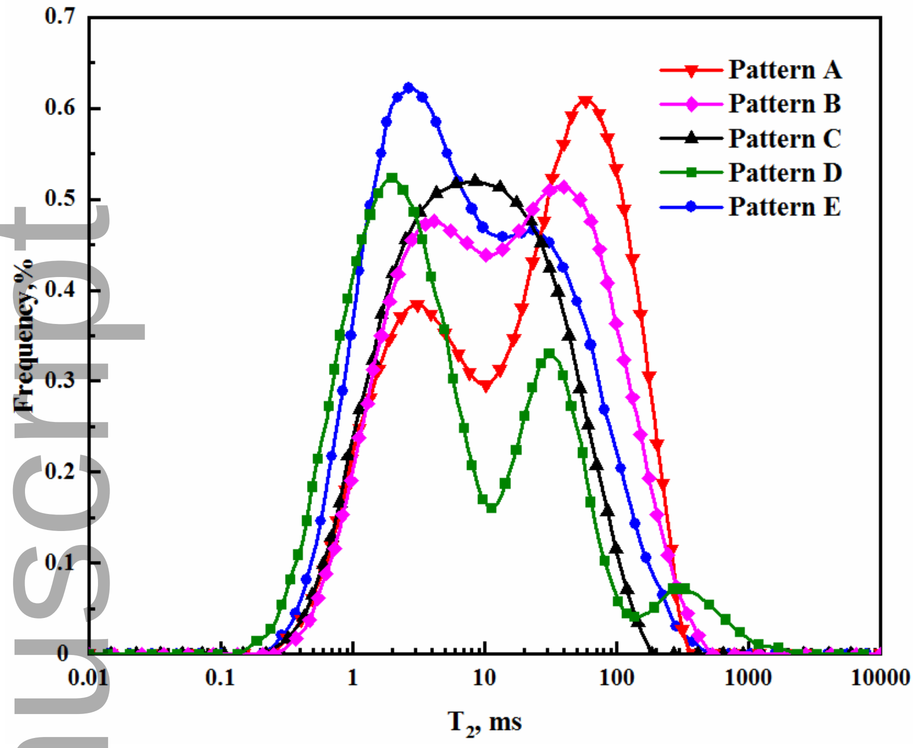

Figure 7. Typical T2 spectrum of five ultra-low permeability sandstone cores. Both Pattern A and B are fine-medium grain feldspar sandstone; Pattern C and D are fine grain feldspar sandstone; Pattern E is medium-fine grain feldspar sandstone. [57]

The irreducible water saturation in porous media can be also determined by NMR after the centrifugal experiment. The nuclear magnetic signal of oil and water can be separated by using deuteroxide (or water with paramagnetic mediums), hence oil saturation in porous media can be rapidly determined by NMR. The pore structure at almost any scale can be measured with NMR theoretically, and the testing process of NMR is harmless to the porous media. However, the signal can be easily affected by magnetic materials and testing temperature. The distribution of pore radius can only be calculated by the T_2 spectrum after the conversion factor is determined, which varies from different samples. And NMR is deficient in detail reflection of pore structure, such as the distribution of microfracture.

2.1.3. Gas adsorption method

Gas adsorption method is based on Langmuir single molecule adsorption theory.[58] The isothermal adsorption of gas under low temperature and low pressure can effectively reflect the distribution of micropores and mesoporous. Brunauer et al. established the multi-molecular layer adsorption theory based on the single molecule adsorption theory (BET theory), which is one of the most commonly used theory of gas adsorption in porous media.[59] BET isothermal adsorption theory can be expressed by **Equation (5)**.

$$\frac{P}{V_e\left(P_0-P\right)}=\frac{1}{V_{ms}C}+\frac{C-1}{V_{ms}C}\frac{P}{P_0} \tag{5}$$

where V_e is the equilibrium gas adsorption capacity, and V_{ms} is the monolayer saturation adsorption capacity. P means the equilibrium pressure, and P_0 represents the saturated pressure of gas. C is the BET constant which can be calculated by **Equation (6)**.

$$C=e^{\frac{E_1-E_L}{R_hT}} \tag{6}$$

where E_1 is the adsorption heat of the first layer, E_L is the adsorption heat of other layers except for the first layer. R_h means the molar heat capacity, and T denotes the test temperature.

N_2 and CO_2 are generally used as the adsorption gas to characterize pore structure of porous media. CO_2 can enter into the smaller pore because of smaller molecular diameter compared with N_2, and CO_2 is easier to reach saturation adsorption state than N_2 owing to the slower diffusion velocity. Therefore, the measurement range of CO_2 adsorption is broader than N_2 adsorption.[60] The isothermal adsorption curve and isothermal desorption curve are obtained by measuring gas adsorption capacity under different pressure conditions, and the pore characteristic parameters can be further calculated according to relevant mathematical models. The specific surface area is calculated using the BET method, and the pore volume can be obtained using the Barrette-Joynere-Halenda (BJH) method.[61],[62] Pore radius can be calculated by **Equation (7)**.

$$r=-\frac{2C_0V_m}{RT_b\ln\left(P/P_0\right)} \tag{7}$$

where r is the pore radius, and C_0 is surface tension at gas boiling point. V_m is the molar volume of gas. R is the gas constant, and T_b is the boiling temperature of gas. P is the equilibrium pressure, and P_0 is the saturated pressure of gas.[63]

Figure 8 a shows the CO_2 isothermal adsorption curve for the Longmaxi shale sample (Type I), implying the presence of micro-pores. **Figure 8** b indicates the pore volume distribution curve obtained by CO_2 adsorption for the shale sample. The pore diameter varies from 0.3 nm to 1.5 nm, and there are mainly three peak values of 0.33-0.37 nm, 0.5-0.55 nm, and 0.57-0.63 nm.[64]

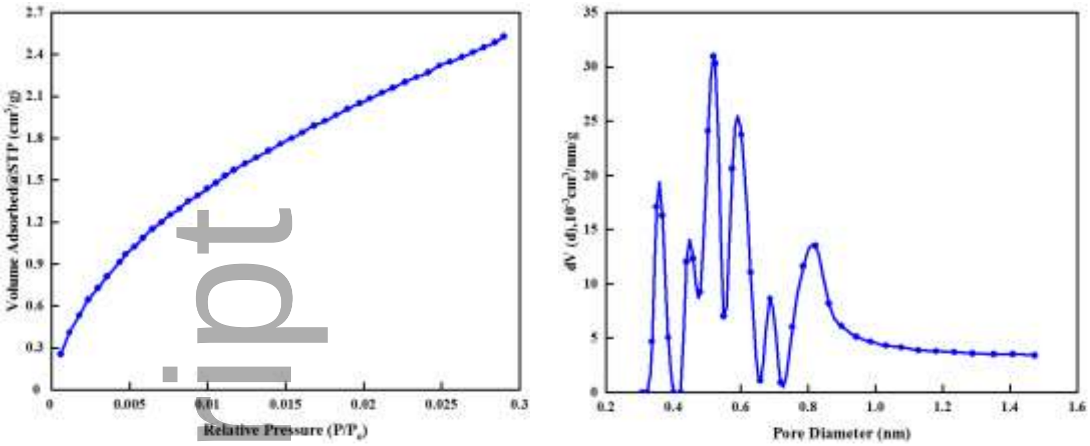

(a) (b)

Figure 8. Curves of CO_2 adsorption for the Longmaxi shale. (a) Low pressure CO_2 isothermal adsorption; (b) Pore volume distribution obtained by CO_2 adsorption.[64]

Nano-scale pore can be characterized using gas adsorption. However, the pore structure measured by gas adsorption may only reflect characteristics in limited areas of porous media due to few experiment data, and the characterization of macropores by gas adsorption is not accurate. The combination of molecular simulation method and gas adsorption method have also been used for pore structure characterization.[65]-[67]

In conclusion, MIP is the traditional method to characterize the pore structure, but only micron-scale pores can be detected effectively. Nano-scale pores can be observed using NMR and gas adsorption. However, only limited characteristic of pore structure can be described using gas adsorption. The pore structure at almost any scale can be detected by NMR theoretically, thus a broad application of NMR is proposed in pore structure characterization.

2.2. Image analysis

The pore structure of porous media can be directly and accurately observed by image analysis. These methods mainly include cast thin sections, scanning electron microscopy (SEM), X-ray computed tomography (CT). **Table 2** gives the difference among three image analysis of pore structure characterization. The minimum measurement range of thin section is only microns, while SEM and X-ray CT can measure nanoscale pore structure. Three-dimensional (3D) pore and throat distribution can be acquired using X-ray CT, while only two-dimensional (2D) images can be detected by thin section and SEM. Thin section has advantages in testing costs.

Table 2. Details on the various image analysis of pore structure characterization.

Techniques	Measurement range	Method of measurement	Parameters	References
Thin section	1 μm -1 mm	Mineral and pore characteristics are observed by the microscope after staining.	2D pore types, pore shape, pore connection relation, mineral types, cementation types.	[68],[69]
SEM	1 nm – 1 mm	Pore structure and composition of the sample are characterized by the secondary electron.	Pore size, pore connection relation, mineral composition, cementation mode.	[70]
X-ray CT	10 nm –10 mm	Slice images are captured by the penetrating X-ray.	3D pore size distribution, spatial connectivity, and mineral composition.	[64]

2.2.1. Thin section analysis

Image analysis based on thin sections of cores is one of the most commonly used techniques in geological exploration and development for oil and gas resources. 2D thin section of micron-scale is manufactured through core cutting, grinding, polishing. Pore structure, mineral characteristics and cementation type of thin section can be directly observed with optical microscope. Mineral composition can be determined according to the optical characteristics of different minerals in the thin section.[71]

The pores in the thin section are highlighted and distinguished from the rock matrix by staining.[72] **Figure 9** shows thin section images of six different sandstone, in which the mineral composition and pore structure can be clearly observed. Primary intergranular pores are distributed in sandstone (**Figure 9** a, b). And dissolved pores can also be found in sandstone (**Figure 9** c, d). Due to the extensive compaction and cementation, particles of fine sandstone and siltstone are smaller, and primary intergranular pores are rare (**Figure 9** e, f).

Initially, thin section is observed by a microscope, and the parameters are recorded manually to calculate the pore structure parameters of the rock.[73] Obviously, large errors are easily caused by the manual observation. Automatic analysis based on has been introduced into thin section analysis to improve its accuracy.[74]-[76]

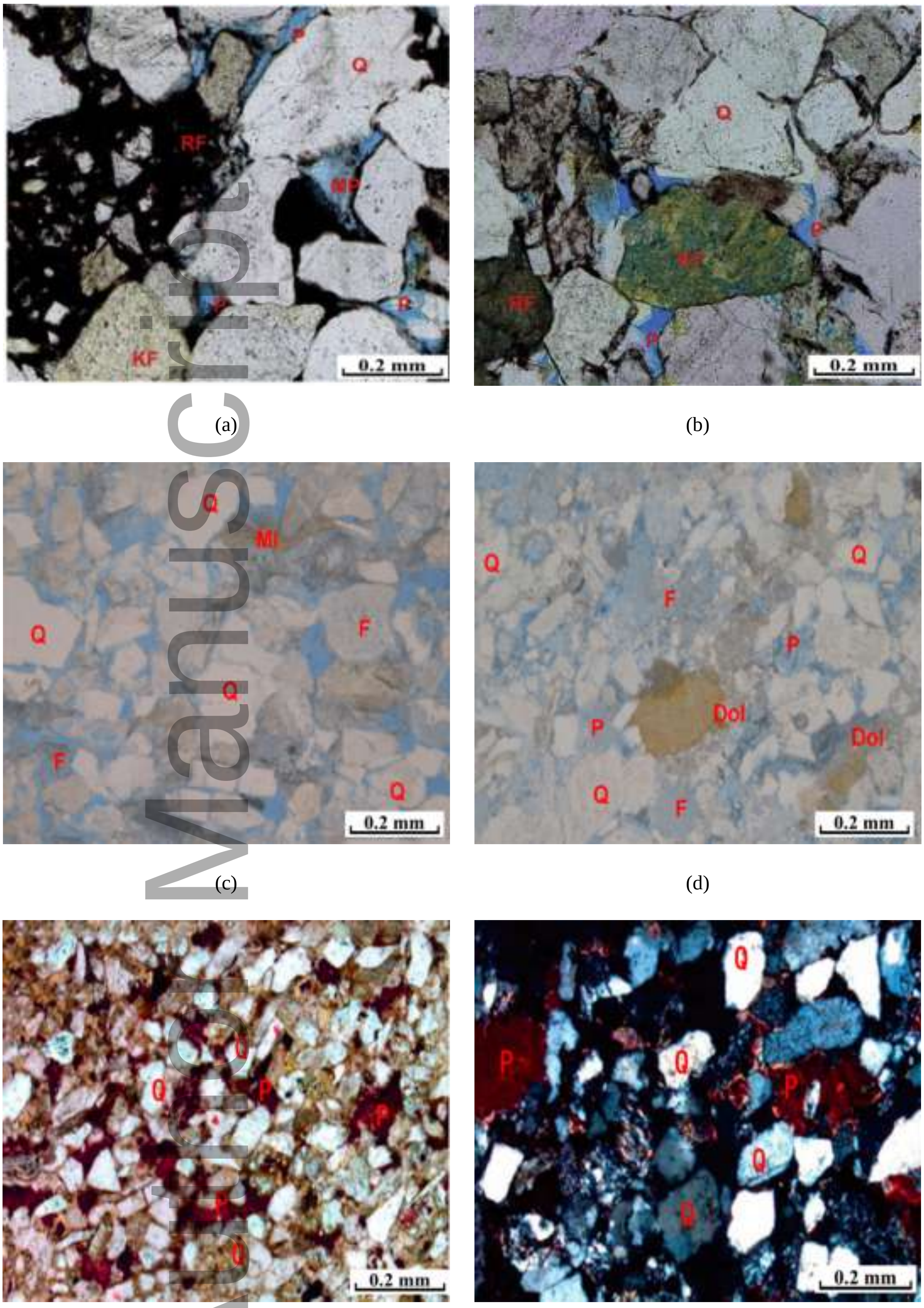

(a) (b)

(c) (d)

(e) (f)

Figure 9. Thin section images of sandstone.[77]-[79] (a) White Feldspathic quartz sandstone, most of the pores are intergranular primary pores; (b) Feldspathic lithic quartz sandstone, with intergranular primary pores; (c) Feldspathic quartz sandstone, pores are mostly intergranular primary pores with few dissolved pores; (c) Feldspar dolomitic quartz sandstone, most of the pores are intergranular primary pores; (e) Brown red fine sandstone, most of the pores are intergranular dissolved pores; (f) Grey siltstone, most of the pores are intergranular dissolved pores. Q = quartz; P = pores; F = Feldspar; RF = rock fragments; MP = macropores; MI = Mica KF = K-feldspar grains; Dol = dolomite.

Thin section analysis is easy to operate and cost effective. It has been widely applied in the analyzing distribution and connectivity of pore and throat. However, measurement range of thin section can only reach micron level, and the preparation of thin section may lead to the loss of the small clay particles of core samples due to washing oil.

2.2.2. Scanning electron microscopy

The scanning image of solid surface can be obtained by the secondary excitation of electron beam on the sample surface using SEM. It can be used to investigate the pore structure and mineral composition of rock.[80] Secondary electron (SE) is emitted by incident electrons that generate inelastic scattering in the sample. Generally, the energy of SE is less than 50 eV and the generated depth of SE is within 10 nm on the sample surface. Therefore, SE is sensitive to the morphology and composition of sample surface so that microscopic characteristics can be reflected by SE.[81],[82] **Figure 10** represents the micro images of three sandstones with different grain sizes measured by SEM. The pores and roar are smaller and less obvious in the denser sandstone.

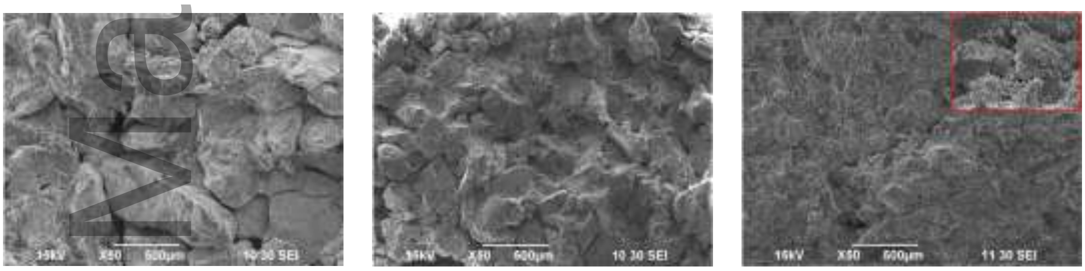

(a) (b) (c)

Figure 10. Environmental SEM images of the tight sandstone. (a) Coarse grain sandstone; (b) Medium grain sandstone; (c) Fine grain sandstone.[80]

High sample quality (e.g., cleanliness, humidity, and electrical conductivity) is required for conventional SEM. A vacuum environment is required during obtaining images, and a conductive coating is needed on the surface of non-conductive samples to eliminate the influence of noise. The sample preparation is complicated, and the observed image of the processed sample is the characteristic of the coating on the surface, which is not totally the same with the sample surface. SEM techniques are gradually improved for core pore testing, including environmental scanning electron microscopy (ESEM), field emission scanning electron microscopy (FE-SEM), and focused ion beam scanning electron microscopy (FIB-SEM).[83],[84] The SEM image is high-resolution, stereoscopic and accurate, and the SEM is convenient. Therefore, it is suitable for observing the rough surface of the core. However, the testing process of SEM may cause damage to the sample surface.

2.2.3. X-ray CT

2D images of the porous media can be captured nondestructively by X-ray CT. Pore structure characteristics are analyzed using mathematical and computer methods. 3D image of the porous media can be established with the 2D images obtained by X-ray CT.

CT scanning is firstly used in the medical field. Now it has been widely applied in several non-medical fields, such as engineering, geophysics and materials science.[85],[86] Nano-CT and micro-CT techniques can quickly detect clear rock images. The internal structure and fluid distribution can be observed owing to the high penetration efficiency of X-ray, and the characteristic parameters can be calculated quantitatively based on these images. **Figure 11** shows the slice of a 3D image of sandstone core measured by X-ray CT. Pores and grains can be clearly found in original image (**Figure 11** a), and various fluids in the core can be distinguished after the image is processed (**Figure 11** b).

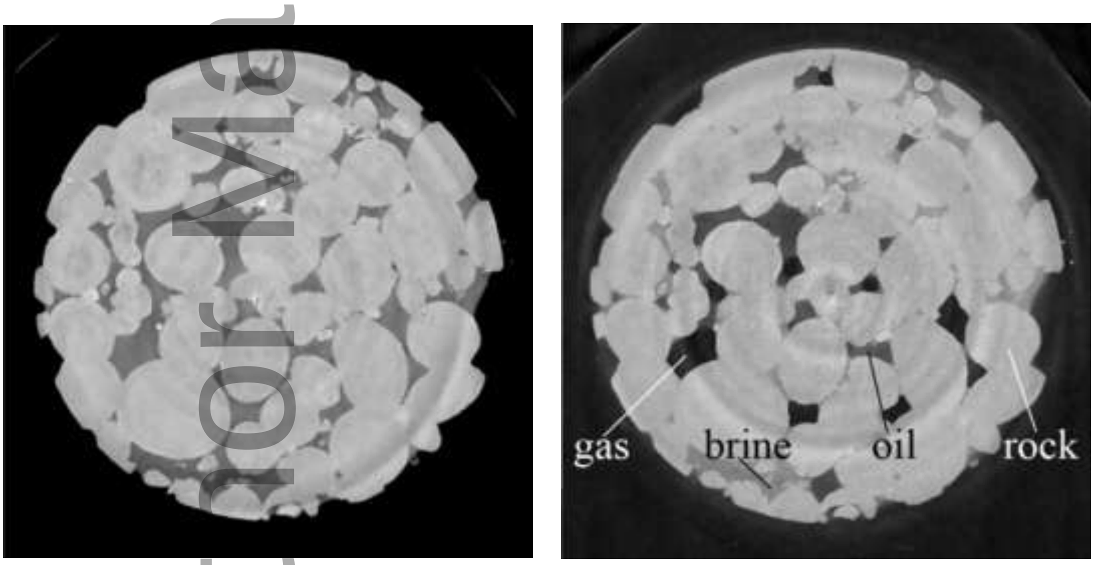

(a) (b)

Figure 11. Slices of a 3D image of sandstone core. (a) The original image; (b) The processed image.[87]

Pore structure characteristic of porous media can be nondestructively and quickly captured based on 3D images obtained by X-ray CT. However, the minimum pore can be observed using X-ray CT is about 10 nm.

In conclusion, thin section analysis is most commonly used to characterize the pore structure of porous media, however the minimum of measurement range is only in microns. Nano-scale pores and throats can be observed using SEM, while damages are caused for the porous media sample. 3D characteristic of pore structure can be obtained by X-ray CT. Therefore, the application of X-ray CT is increasing for image analysis.

2.3. Digital core technique

Digital core technique refers to the technology of simulating the pore structure in the core by computer, which can construct and model the pore structure of the rock without destroying the original core. It makes up for the shortage of petrophysics experiment. All properties of core sample will not be affected by using the digital core. Physical experiments and numerical methods are generally adopted in the reconstruction of 3D digital core.[88]

The main physical experimental methods for the establishment of digital core include sequence imaging, focused laser scanning and X-ray CT scanning. The sequential imaging method is to repeatedly cut and polish the core surface to obtain a series of microstructural images, and the 3D visual digital core can be obtained by stacking images in order.[89] Sequential imaging can characterize nanoscale cores , but it is hardly used since the experimental process takes a lot of time and the cores may be damaged. In confocal laser scanning method, thin section of core injected with dyed epoxy resin are scanned, and the reflection intensity is recorded and converted into gray signal to generate core images.[90]-[92] However, the obtained digital core thickness is small and close to 2D by confocal laser scanning method so that it is hard to reflect the 3D feature of cores, which is also rarely used. 2D core images are obtained through X-ray CT scanning technology, and images are combined to establish the digital core.[93] This method is harmless to the core microstructure and shows highly accurate imaging results, so that it is commonly used to establish the digital core.[94],[95]

The numerical reconstruction methods for the establishment of digital core consist of stochastic simulation method (e.g., Gaussian simulation, simulated annealing, multipoint statistics)[96]-[99] and process simulation method.[100]-[102] The digital core can be established by the statistical information of core slice images using numerical reconstruction methods. However, the digital core developed by numerical methods is simplified compared to the actual core. **Figure 12** shows the 2D slices of sandstone measured by FIB-SEM and the digital core established with slices.[103] Micropores and microfracture at nano-scale can be seen in **Figure 12** a and b. The distribution of pore and fracture can be intuitively observed in the digital core built by 2D slices

(**Figure 12** c, d).

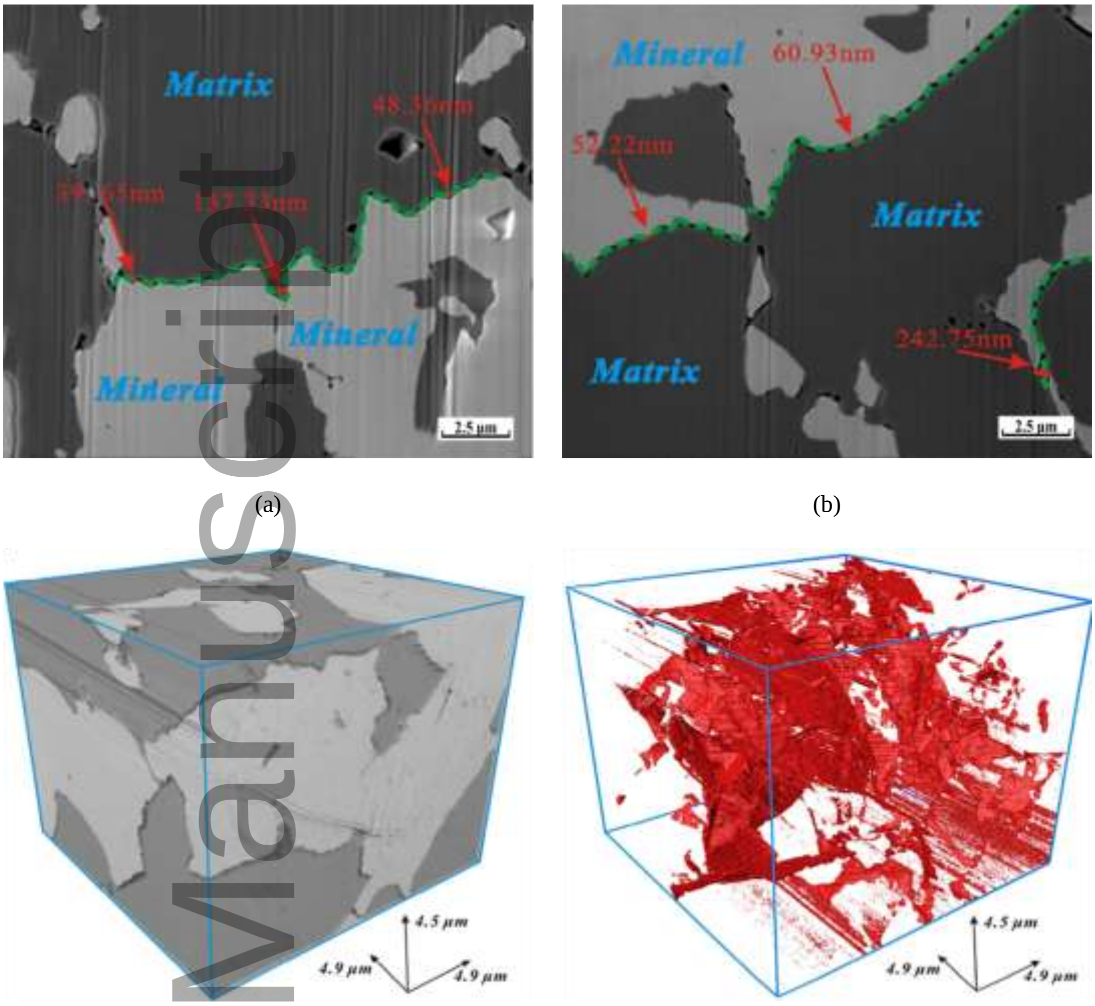

(a) (b)

(c) (d)

Figure 12. The digital core established by 2D FIB-SEM slices. (a) 2D slice at 1 μm in *x* direction; (b) 2D slice at 3 μm in x direction; (c) established digital core; (d) pore and fracture network of the digital core.[103]

The pore structure characteristic can be clearly presented through the digital core. The application of digital core gradually increases because it is reusable and visible. However, the accuracy of the digital core depends on the image's quality used to establish the digital core.

3. Microscopic flow mechanism of CO_2 flooding through experiments

Pore-scale visualization, X-ray CT and NMR are usually used to investigate the microscopic flow mechanism of CO_2 flooding in oil and gas reservoirs. **Table 3** presents the difference among three experiments.

Table 3. Details on the various experiments to research microscopic mechanism of CO_2 flooding.

Techniques	Range	Advantages	References
Visualization experiment	≥ 10 nm	The change of fluids in porous model can be detected directly. The preparation and process of the experiment are simple, and; the cost is low.	[104],[105]
X-ray CT	10 nm – 10 mm	3D digital core can be reconstructed with slices measured by X-ray CT.	[106]
NMR	0.1 nm - 10 mm	The distribution of fluids in porous media can be accurately obtained at full scale.	[107]

3.1. Pore-scale visualization

The displacement process can be directly observed at the pore scale and recorded using camera and microscope. Therefore, the displacement mechanism and quantitative description of flooding process can be carried out using visible methods. It is significant to construct a microscopic visible model to reflect the actual porous media.[104]-[112] **Figure 13** shows the CO_2 flooding process based on a visible porous media model. Brine (colorless) sealed by oil (dark) can be observed at the end of channels after oil injection (**Figure 13** a). CO_2 breaks through along the high-permeability channels due to the distinct difference between oil viscosity and CO_2 viscosity (**Figure 13** b).

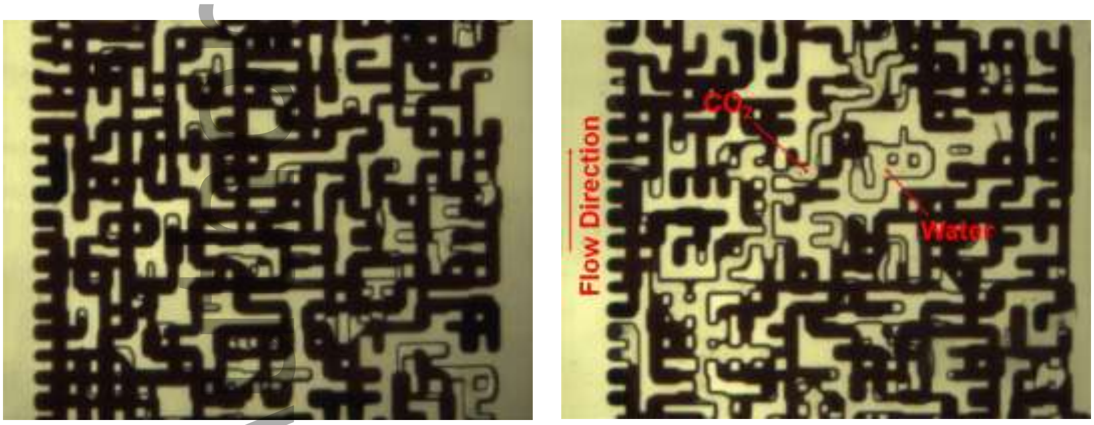

(a) (b)

Figure 13. Schematic diagram of the microscopic visualization model of CO_2 flooding. (a) At the end of the period of oil injection; (b) Before the breakthrough of CO_2.[104]

The process of CO_2 (colorless) displacing oil (yellow) in a visible micromodel is shown in **Figure 14**.[109] The injected CO_2 tends to displace oil in large pores because capillary is a resistance to non-wetting phase (**Figure 14** a, b). CO_2 will flow through a high-permeability channel, and the breakthrough of CO_2 finally appears (**Figure 14** c). The remaining oil is mainly distributed in the small pores and throats and part of the large pores blocked by CO_2 (**Figure 14** d).

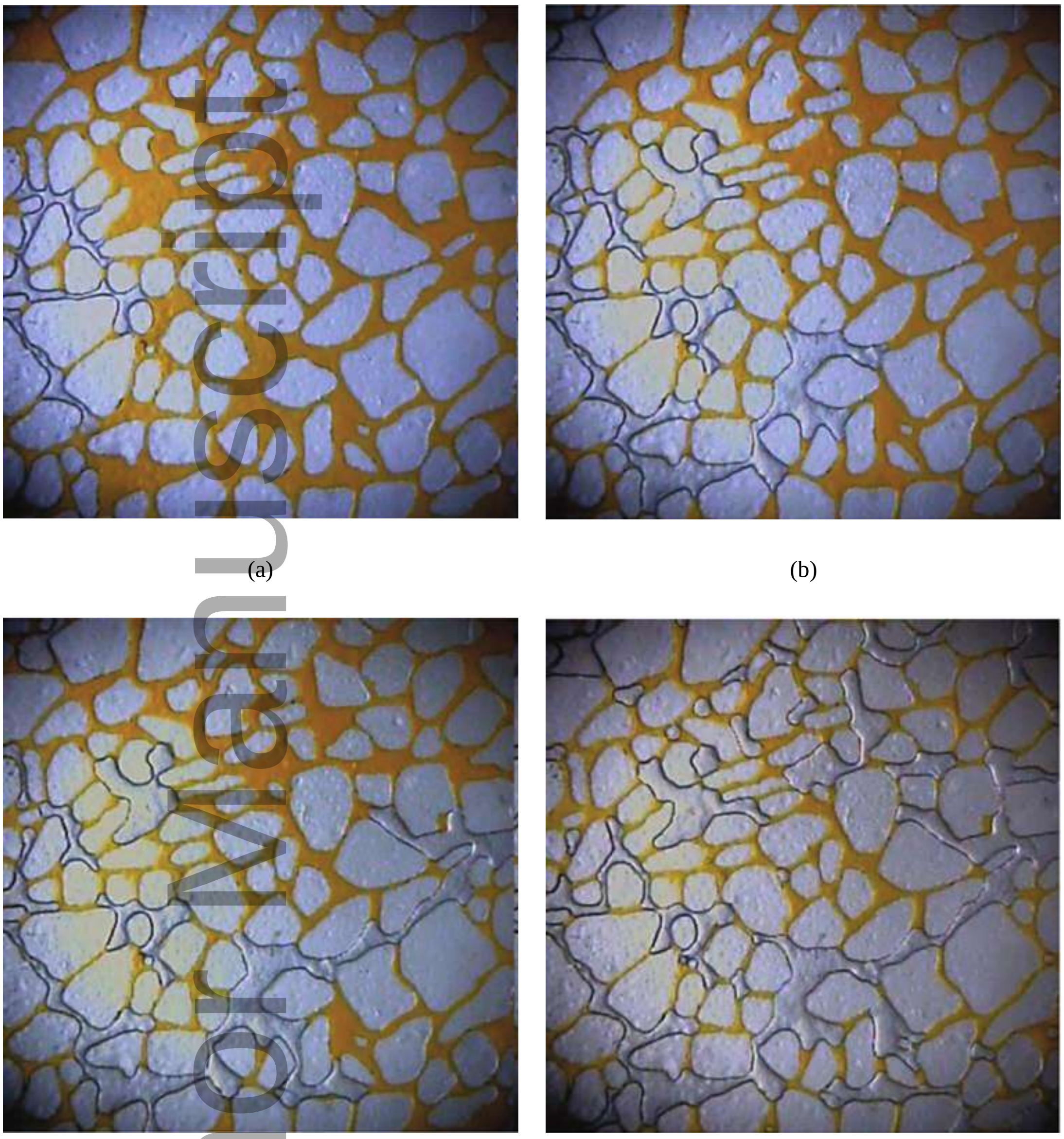
(a) (b)

(c) (d)

Figure 14. Images of CO_2 (colorless) displacing oil (yellow) in the micromodel at injection rate of 0.05 ml/min. (a) 0.1 PV of CO_2 injected; (b) 0.3 PV of CO_2 injected; (c) 0.5 PV of CO_2 injected; (d) 0.7 PV of CO_2 injected [109]

The dynamic contact angle of gas and hydrocarbon in nano-scale channels is shown as **Figure 15**. Hydrocarbon is injected into a nanofluidic chip (**Figure 15** a) with channels of 10 nm depth, and the contact angle is measured using epi-fluorescence images (**Figure 15** b). The contact angle deviates obviously for fluids confined in pore sizes of 10 nm, which means that the fluid flow process at nano-scale is significantly different from the flow at macro-scale.[110]

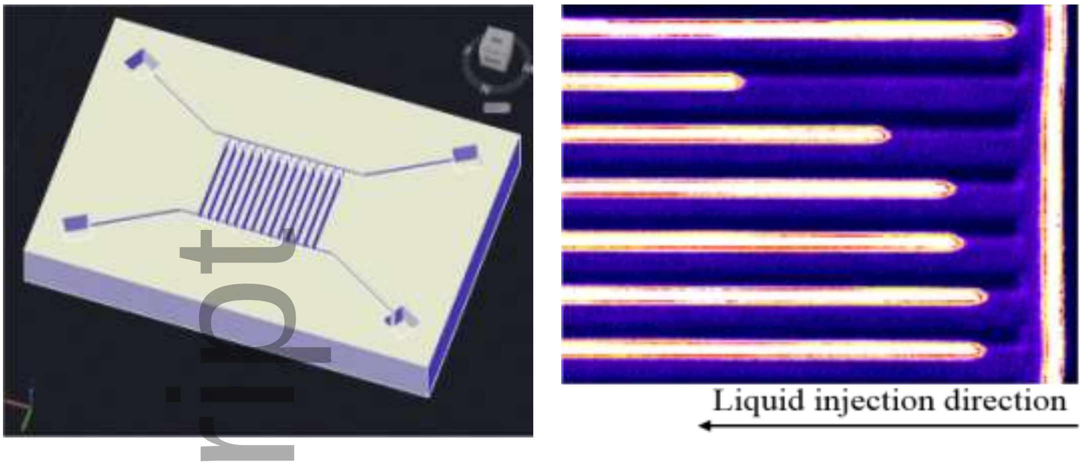

(a) (b)

Figure 15. The dynamic contact angle in a nanofluidic chip: (a) schematic figure of the nanofluidic chip; (b) microscopy images taken from the sample hydrocarbon.[110]

The visual model is mainly composed of glass, acrylic and other materials that are easy to be etched and able to withstand pressure. Furthermore, other models are established by bonding quartz sand or the casting thin sections of actual cores. The smallest pore and throat size of the model can reach nano-scale using etching techniques (e.g., interference lithography, electron beam lithography, polymer nano channels).[113]-[116]

The fluid flow during CO_2 flooding can be obviously monitored by pore-scale visualization techniques. However, there are still challenges including the pressure limitation of the experimental model and difference between the constructed model and reservoir.

3.2. X-ray CT experiments

The intensity of X-ray is reduced after passing through the porous media. The attenuation of X-ray can be converted into electrical signal by the detector, and scanned images can be generated by the computer. The attenuation of X-ray is related to the composition of fluids in porous media. Therefore, the process of CO_2 flooding can be accurately observed using X-ray CT. X-ray CT is an effective method to describe the micropore structure and fluid distribution in porous media intuitively and accurately during displacement experiment.[117]-[120] **Figure 16** shows 2D images of fluid distribution before CO_2 flooding (**Figure 16** a) and after CO_2 flooding (**Figure 16** b) in the sample measured by X-ray CT. The oil in macropores is displaced by CO_2 effectively, and the residual oil is mainly discovered in micropores and channels sealed by the brine.

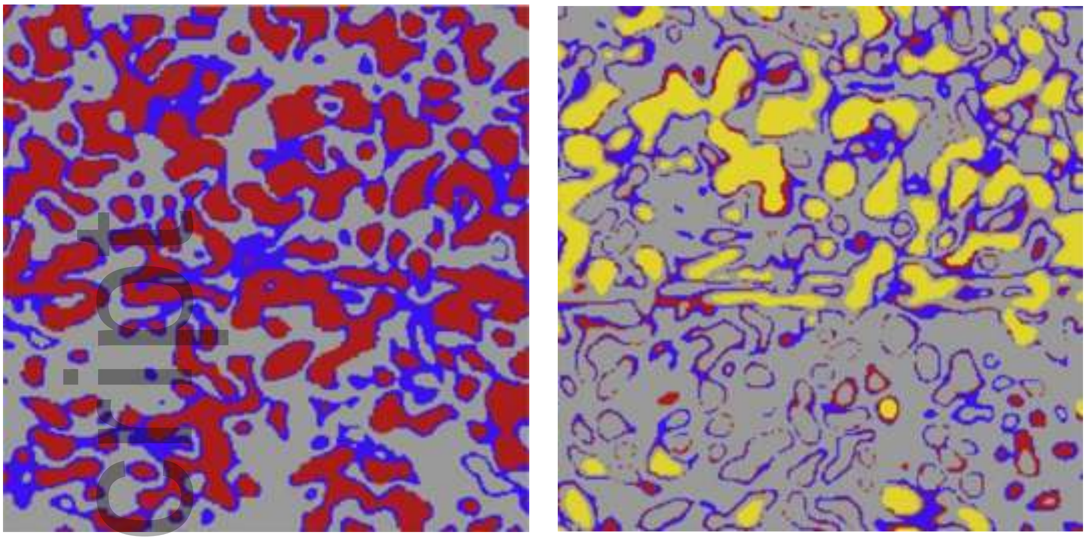

(a) (b)

Figure 16. 2D images of fluid distribution: (a) before CO_2 flooding; (b) after CO_2 flooding. Rock sample is Grey, brine is blue, n-C_{10} is red, and CO_2 is yellow.[117]

2D X-ray CT images of CO_2 displacing brine in a sandstone core simple with horizontal bedding clay layers is shown as **Figure 17**.[118] The displacement direction of scCO_2 and the position of X-ray CT slice are presented in **Figure 17** a. When 0.2 PV of scCO_2 is injected, fingering can be clearly observed (**Figure 17** b). And the scCO_2 breakthrough occurs at 0.6 PV (**Figure 17** c). Two main channels of scCO_2 can be monitored at 2.0 PV, and the residual brine is distributed in the area between the two channels (**Figure 17** d).

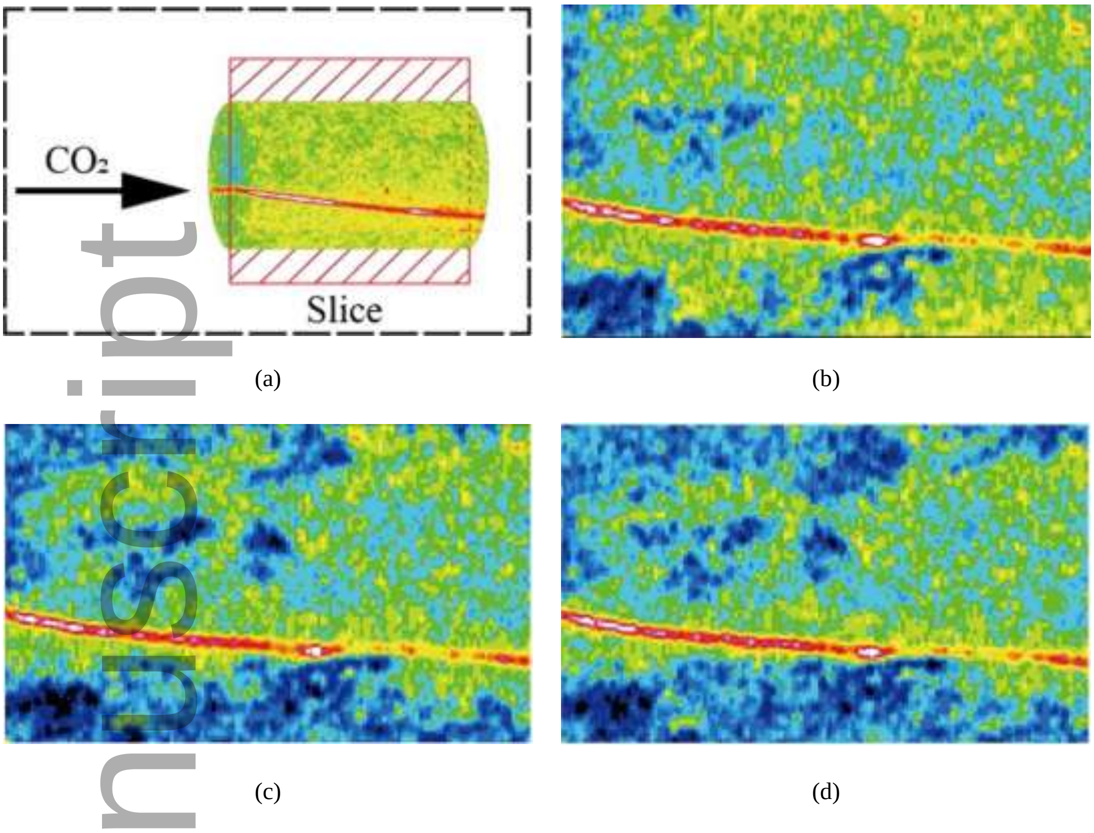

(a) (b)

(c) (d)

Figure 17. 2D images of CO_2 displacing brine measured by X-ray CT. (a) Schematic diagram of displacement direction and slice position; (b) 0.2 PV of $scCO_2$ injected; (c) 0.6 PV of $scCO_2$ injected; (d) 2.0 PV of $scCO_2$ injected. Brine is yellow, $scCO_2$ is blue, and the clay layers is red.[118]

The 3D fluid distribution in porous media can be reconstructed by X-ray CT. And different fluid components can be accurately distinguished. The testing process of X-ray CT is harmless to the sample. However, it takes a longer time and a higher cost than visualization experiment and NMR. Meanwhile, the obtained image data becomes narrower to achieve higher test accuracy.

3.3. NMR experiment

The distribution of fluids in the porous media can be detected by the T_2 spectrum using NMR. The T_2 Relaxation time is directly related to the pore radius of the porous media, thus the fluids presence in pores of different sizes during CO_2 flooding can be represented by the T_2 spectrum.[121],[122] Generally, large pore is related to a long relaxation time and small pore corresponds a short relaxation time.[123],[124] **Figure 18** shows the T_2 spectrum of an ultra-low permeability core (**Figure 18** a) and an extra-low permeability core (**Figure 18** b) during cycling CO_2 injection.[125] The area of the curves above the longer period of T_2 is significantly reduced after CO_2 flooding and soaking, which reflects that the oil in the larger pores is effectively displaced by CO_2.

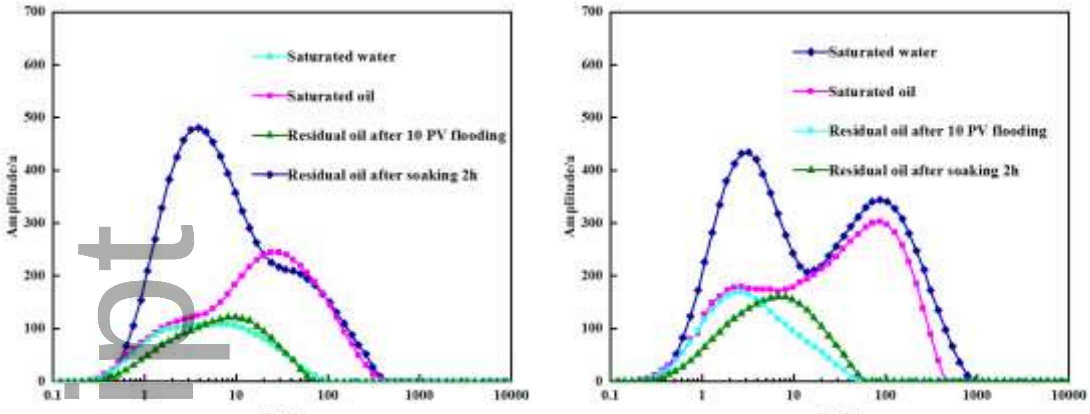

(a) (b)

Figure 18. T_2 curves before and after cycle CO_2 injection: (a) ultra-low permeability core; (b) extra-low permeability core.[125]

2D images of fluid distribution in the porous media can be also measured by using NMR.[126]-[130] Applying two perpendicular gradient magnetic fields in the perpendicular direction to the static magnetic field, different position of the sample will appear diverse responses the pulsed magnetic fields. The internal structure images of the sample can be obtained by recording and processing these signals. The NMR slice images of fluid distribution during water flooding and scCO_2 flooding in a sandstone core are shown as **Figure 19**.[126] A steady piston displacement front can be observed during water flooding (**Figure 19** a, b, c). There is residual oil distributed unevenly in the core after water flooding of 42.90 PV (**Figure 19** c). Then scCO_2 is injected into the core, and the sweep efficiency of scCO_2 flooding is significantly improved and the residual oil is effectively flooding out (**Figure 19** d, e, f).

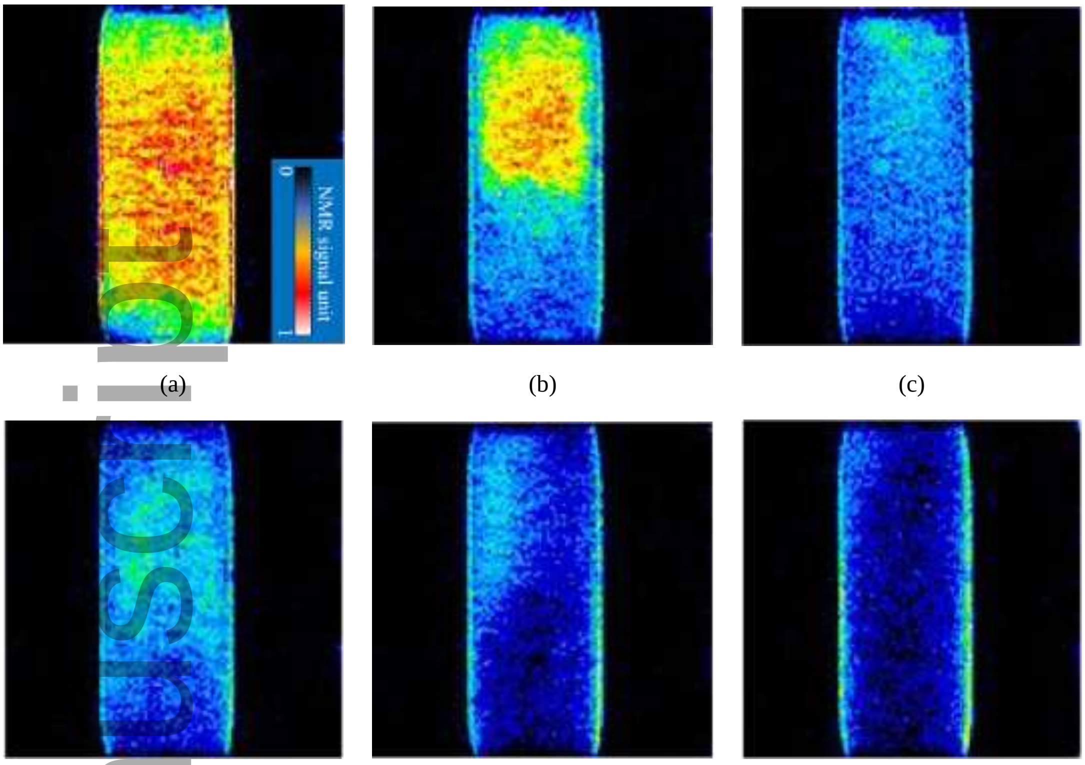

(a) (b) (c)

(d) (e) (f)

Figure 19. NMR images of water flooding and $scCO_2$ flooding at representative time steps in a sandstone core. (a) 0.45 PV of water flooding; (b) 15.63 PV of water flooding; (c) 42.90 PV of water flooding; (d) 44.33PV of $scCO_2$ flooding; (e) 50.86 PV of $scCO_2$ flooding; (f) 62.90 PV of $scCO_2$ flooding.[126]

The pore structure at almost any scale can be measured with NMR quickly and harmlessly with a high precision. However, the process of NMR is sensitive to the test environment. Meanwhile, it is unable to distinguish microfractures from pores by NMR.

In summary, the accuracy of pore-scale visualization is limited by the experimental conditions (e.g., pressure, temperature) and the similarity between the physical model and actual reservoirs. Images of fluid distribution during the process of CO_2 flooding can be obtained using X-ray CT, while the quality of images is limited by the imaging resolution. Fluid distribution can be detected at almost any scale using NMR, but the pore radius calculated by the T_2 is related to the conversion coefficient. Currently, X-ray CT and NMR are preferred to understand the microscopic flow mechanism in porous media. The comparative analysis of the three methods is shown in **Table 4**.

Table 4. Comparison of three experimental methods to understand microscopic flow mechanism of CO_2 flooding

Techniques	Range	Test methods	Advantages	Disadvantages
Visualization experiment	≥10 nm	Direct observation of visual experimental models	Image data is easy to be recorded; the fluid distribution and morphology can be obtained accurately.	The test range is smaller than X-ray CT and NMR; the results depend on graphics processing techniques; test temperature and pressure are limited by the model materials.
X-ray CT	1 nm – 10 mm	Projected data of porous media is obtained by X-rays	The 3D fluid distribution in porous media can be reconstructed; different fluid components can be accurately distinguished; it is nondestructive.	The test takes longer time than visualization experiment and NMR; high test cost; the obtained image data becomes narrower to achieve higher test accuracy.
NMR	0.1 nm -10 mm	The relaxation time of the fluid in the porous media is obtained	The fluid distribution in almost all sizes of pores and throats can be obtained; fast test speed and high precision; nondestructive	Unable to distinguish microfractures from pores; High precision images of fluid distribution cannot be obtained; The test is sensitive to the test environment.

4. Numerical modelling of CO_2 flooding

The fluid transport can be characterized using three approaches, including molecular dynamics (MD) on the microscopic scale, lattice Boltzmann method (LBM) on the mesoscopic scale, and computational fluid dynamics (CFD) method on the macroscopic scale. However, CFD method is based on the continuous medium hypothesis, which is unsuitable at pore-scale. Meanwhile, CFD method is hard to describe the boundary conditions, which is significant to the flow at pore-scale. Therefore, CFD method is hardly used to simulate the flow process at pore-scale. MD and LBM are mainly used to simulate CO_2 flooding in porous media.

4.1. Molecular dynamics simulation

MD simulation is to model the physical and chemical properties of a molecular system. Based on the basic principles of MD, a set of models (e.g., elementary physical model, COMPASS force field, and MSM force field) and algorithms (e.g., Beeman algorithm, Geer algorithm, and Verlet velocity algorithm) are constructed to calculate the reasonable molecular structure and behavior.[131]-[136] MD simulation starts from the actual physical process of fluid molecular motion, and the displacement, velocity, force and other changes between molecules at any time are further analyzed according to Newton's law of motion. Finally, statistical methods are applied to obtain macroscopic characteristics, such as macroscopic velocity and pressure. MD simulation is based on the basic motion law of classical mechanics. In principle, it can simulate any fluid system without making prior assumptions about transport parameters and thermodynamic behavior.[137]

The key idea of molecular dynamics is to obtain the change of particle position by solving the motion equation of each particle based on the classical Newtonian mechanics law **(Equation (8))**.

$$m_i \frac{d^2 r_i(t)}{dt^2} = -\sum_{i<j} \frac{\partial V(r_{ij})}{\partial r_{ij}} \tag{8}$$

where m_i is the mass of Particle i, r_i means the position vector of Particle i. $V(r_{ij})$ represents the interaction potential function of Particles i and j, and r_{ij} denotes the relative position between Particles i and j. t is the time.

The motion of a particle at different time steps using MD simulation is shown in **Figure 20** a. The calculation process of MD simulation can be found in **Figure 20** b. The initial conditions (e.g., temperature, pressure, time step) of particle system are firstly determined, and each particle is given a random velocity. Secondly, the force and acceleration on each particle can be calculated. Thirdly, the position of each particle in the system in the next time step is calculated according to the **Equation (8)**. The fourth step is to calculate the force and acceleration of the particle again, and repeat it until the desired result is achieved. Finally, the thermodynamic characteristics, adsorption characteristics, diffusion and migration characteristics of the model system can be understood.[138]

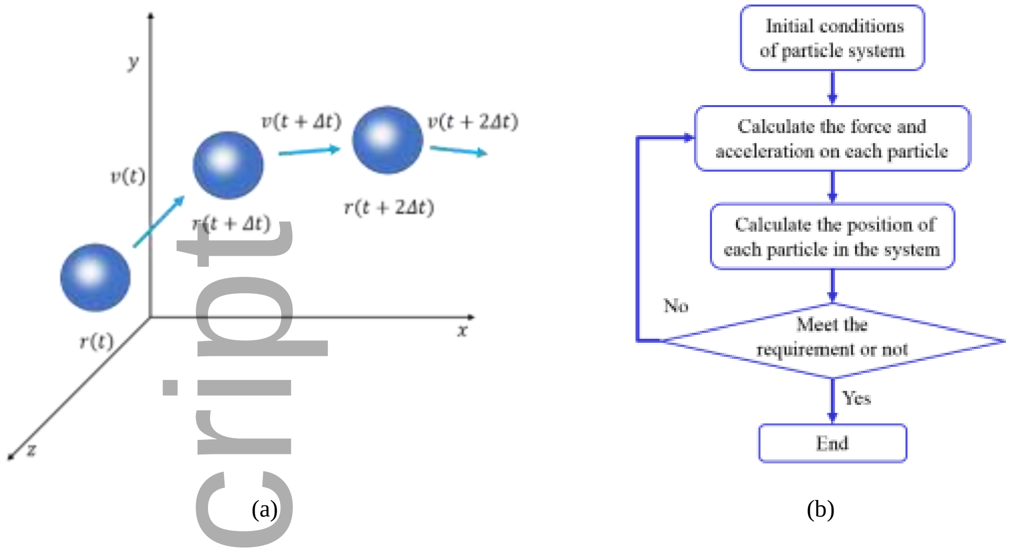

Figure 20. (a) The position and velocity of particle at different time steps; (b) Workflow of MD simulation.[138]

In recent years, MD simulation technology has been used increasingly in understanding hydrocarbon flow phenomena in porous media and the phase behavior of mixed fluids at nanoscale.[139]-[141] **Figure 21** shows the changes of particles during oil displacement by using various mediums. The interaction between oil and gas leads to different displacement performance. The dissolution of gas and oil and displacement occur almost at the same time, and there are still a lot of residual oil adsorbed on the solid surface, shown in **Figure 21** a. Mass transfer occurs between CO_2 and oil and a miscible zone is formed, while N_2 pushes the whole miscibility zone forward, resulting in high displacement efficiency (**Figure 21** b). For the slug flooding (CO_2 and N_2), the breakthrough of N_2 slug occurs quickly and a large amount of residual oil is remained on the solid surface as shown in **Figure 21** c. However, the residual oil can be adequately extracted by CO_2.[142] **Figure 22** indicates the miscible process of C_3H_8 and $C_{10}H_{22}$ using MD simulation. The interface between C_3H_8 and $C_{10}H_{22}$ can be clearly observed at 0 ns (**Figure 22** a). Several molecules dissolve in oil phase and few molecules exist in gas phase at 0.25 ns (**Figure 22** b) due to the faster movement of gas molecules. The miscibility degree of gas and oil phase increases with time (**Figure 22** c-f)[143]

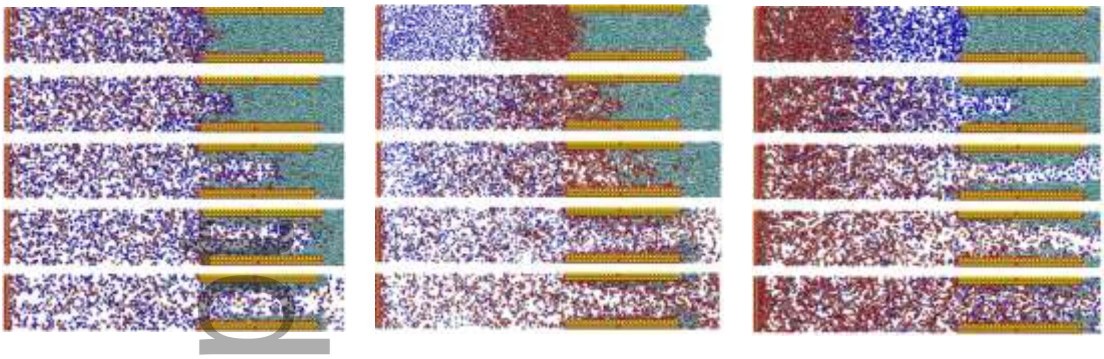
(a) (b) (c)

Figure 21. Snapshots of oil displacement by different mediums using MD simulation. The time from top to bottom is 0 ns to 2 ns. (a) Mixed gas; (b) CO_2 slug and N_2 ;(c) N_2 slug and CO_2. Oil is green, CO_2 is red, and N_2 is blue.[142]

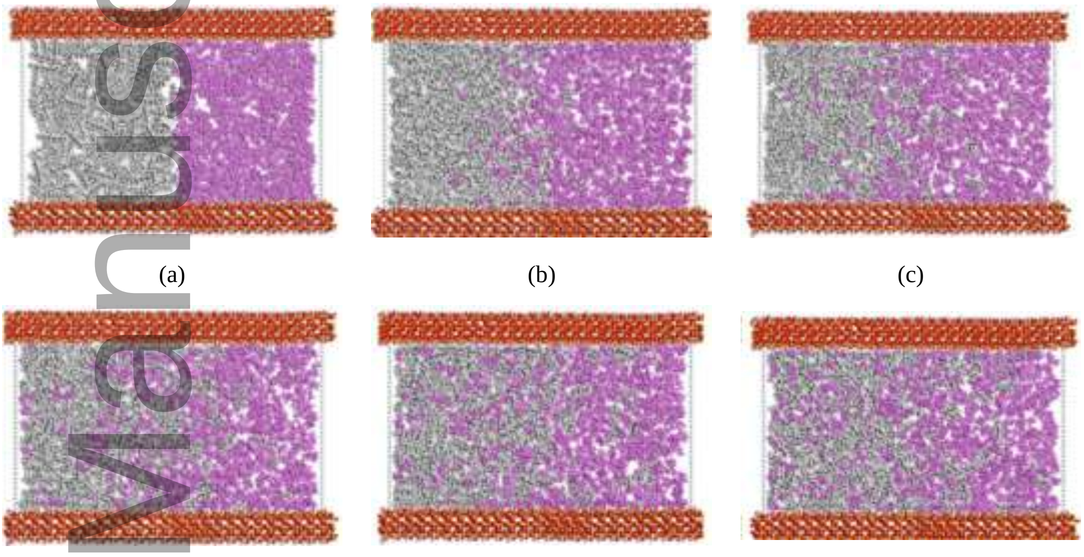
(a) (b) (c)

(d) (e) (f)

Figure 22. Molecular dynamics simulation of C_3H_8 (purple) and $C_{10}H_{22}$ (gray)miscible process at 400K and 0.056GPa: (a) Time = 0 ns; (b) Time = 0.25 ns; (c) Time = 0.5 ns; (d) Time = 1 ns; (e) Time =1.5 ns; (f) Time = 2 ns.[143]

MD simulations can numerically model fluid flow at various molecular scales theoretically. However, it requires huge computing time and resources for molecular dynamics simulation of macroscopic flow due to the large number of molecules in the fluid. Meanwhile, it is hard for MD simulation to deal with the irregular boundaries, and construct the molecular potential function.

4.2. Lattice Boltzmann Method

LBM links macroscopic fluid mechanics with microscopic molecular dynamics based on the lattice gas automata, molecular kinetic theory and statistical physics. [144]-[146] The macroscopic partial differential equation is needless for LBM to understand the flow mechanism.[147] The flow system is represented by spatial discrete model and velocity discrete model of particles. The model space is divided into lattices. Particles exist between the lattices, and particles migrate along the lattice lines and collide at the lattice points. The motion process of particles follows the mechanics rules and the statistics rules. The macroscopic motion variables of the fluids can be obtained by calculating the statistical average of a large number of particles in the flow field.[148],[149] **Figure 23** shows slices of fluids distribution in CO_2-brine displacement using LBM at different time steps.[150] The brine is partly displaced by $scCO_2$. Small pores are occupied by the brine, which is surrounded and trapped by $scCO_2$ in macro pores.

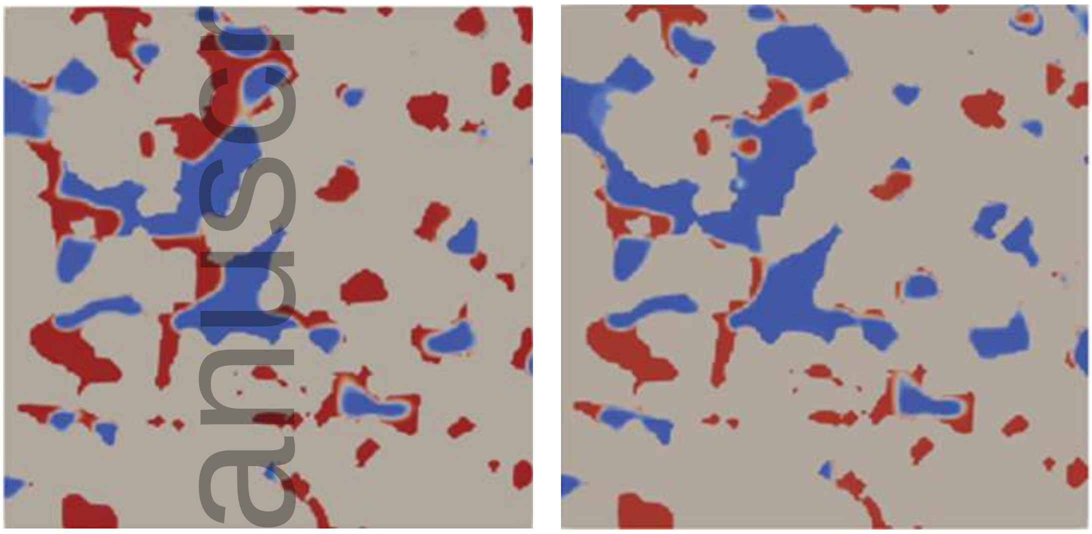
(a) (b)

Figure 23. Phase distribution of $scCO_2$ at a single slice along the flow direction in the simulation of $scCO_2$–brine immiscible displacement by using LBM. $scCO_2$, brine and solid skeleton are marked in blue, red and gray, respectively. (a) at time steps 200000; (b) at time steps 800000.[150]

The LBM is derived from the Lattice Gas Automata (LGA) model which is mainly used in the field of fluid mechanics.[151],[152] The calculation of LGA is paralleled and stable so that LGA is suitable for large parallel operations. However, large amount of computing resources is required due to the statistical noise and the complex collision operator. The single relaxation Boltzmann model is established by simplifying the collision matrix based on the Bhatnagar-Gross-Krook (BGK) collision interval theory[153],[154], which is referred as Lattice BGK (LBGK) model. LBGK overcomes the defects of LGA gradually become widely used in numerical simulation. The Navier-Stokes (N-S) equation can be derived by LBGK with Chapman-Enskog method. D_nQ_b model[155],[156] is the most widely used among LBGK, as shown in **Figure 24**.

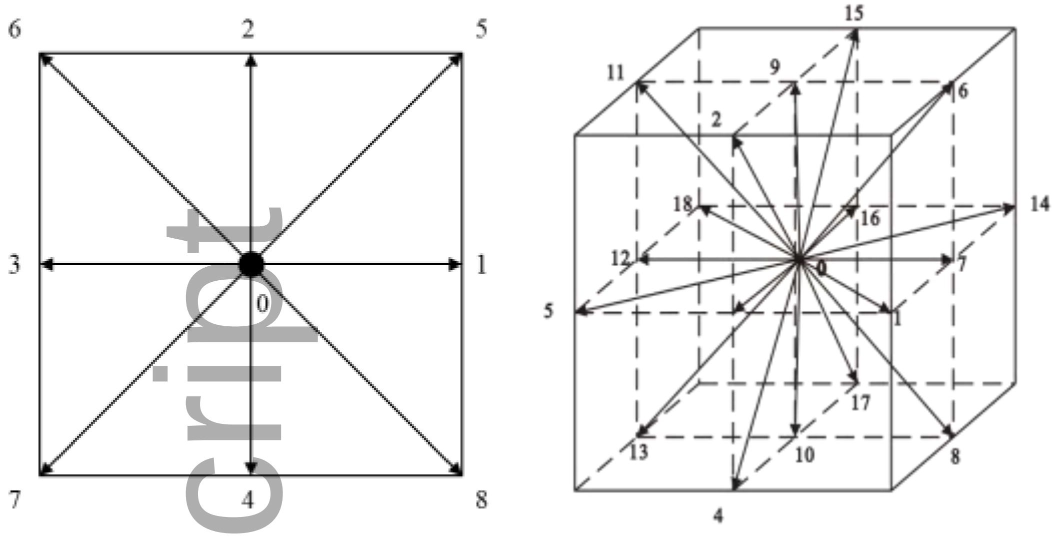

(a) (b)

Figure 24. Models of D$_n$Q$_b$: (a) D$_2$Q$_9$ model; (b) D$_3$Q$_{19}$ model.

The discrete velocity of D$_n$Q$_b$ model can be expressed by **Equation (9)**.

$$f_i(x + c_i\Delta t) - f_i(x,t) = -\frac{1}{\tau}\left(f_i(x,t) - f_i^{eq}(x,t)\right) \tag{9}$$

where $f_i(x,t)$ is the density distribution function at x space position and i velocity direction at time t. τ is the dimensionless relaxation time. $f_i^{eq}(x,t)$ is the equilibrium density distribution function which can be described by **Equation (10)**.

$$f_i^{eq}(x,t) = \omega_i\rho\left[1 + \frac{c_i \cdot u}{c_s^2} + \frac{(c_i \cdot u)^2}{2c_s^4} - \frac{u^2}{2C_s^2}\right] \tag{10}$$

where ω_i is the coefficient related to the length of a vector in the direction of discrete velocity.c_i means the discrete lattice velocity, and C_s denotes a constant associated with the dimensions of space. ρ represents the macro density, and u is the macro velocity.

The model satisfies conservation of mass and momentum, which can be described by **Equations (11)** and **(12)**.

$$\rho = \sum_i f_i(x,t) = \sum_i f_i^{eq}(x,t) \tag{11}$$

$$\rho u = \sum_i f_i(x,t)e_i = \sum_i f_i^{eq}(x,t)e_i \tag{12}$$

where e_i is the component of the macro velocity in the discrete direction.

MD simulation requires a large amount of computing resources to model flow in porous media.

The calculation of LBM is efficient and accurate in numerical simulation for CO_2 flooding at pore-scale. Therefore, it’s better to use LBM to understand the microscopic flow mechanism of CO_2 flooding.

5. Conclusions

This paper presents an overview of pore structure characterization and microscopic flow mechanism during CO_2 flooding in porous media.

(1) The pore structure of rock can be characterized through experimental analysis (i.e., MIP, NMR, gas adsorption), image analysis (i.e., thin sections, SEM, CT), and digital core technique. The pore structure description by experimental methods is indirect so that it is sensitive to the calculation models. Image analysis can capture pore structure images directly, but it is difficult to characterize it quantitatively. Digital core reflects the 3D pore structure and properties of actual porous media, and can be used repeatedly while keeping the same characteristics. Therefore, digital core approach shows broad application potential for pore structure characterization since it is reusable and visible. However, the accuracy of the digital core depends on the images’ quality and needs to be further enhanced.

(2) Pore-scale visualization, X-ray CT and NMR are usually applied to investigate the microscopic flow mechanism of CO_2 flooding in oil and gas reservoirs. The process of CO_2 flooding can be directly observed using pore-scale visualization, so that the fluid distribution and mass transfer can be analyzed qualitatively. Nano-scale visual models can be made using etching techniques, which is significant to investigate the flow process of CO_2 flooding in unconventional reservoirs (e.g., extra-low permeability reservoir, shale reservoirs). The fluid distribution can be accurately detected by both X-ray CT and NMR to understand the microscopic flow mechanism during CO_2 flooding in porous media. However, NMR is unable to obtain the distribution feature for individual phase fluid within single test, and the fluid flow in microfracture and pore are difficult to be distinguished. The authenticity of X-ray CT images is affected by the selected threshold value during image processing. The flow experiment can represent the flow process in detail, while it is limited by physical conditions and similarity between the physical model and actual reservoirs. Future work can be done to improve the materials of visible model to reach higher temperature and pressure in pore-scale visualization.

(3) Fluid transport in porous media can be modelling using MD on the microscopic scale and LBM on the mesoscopic scale. Although MD approach can accurately reflect the flooding process through molecular motion and interaction among molecules, limitations in simple boundaries and huge amount of computation makes it hard to simulate the fluid flow in reservoirs. LBM achieves the parallel computing and can deal with complex boundaries. Therefore, it is efficient in simulating multi-phase fluid flow in porous media, and exhibits promising application in simulating CO_2 flooding in unconventional oil reservoirs. Although numerical model is simplified compared to physical experiments (e.g., NMR, X-ray CT), it is more convenient and repeatable to investigate the effect on microscopic flow by simulation. How to reduce the computational burden of MD and improve the accuracy of LBM for multiphase flow simulation need to be solved.

(4) The pore structure in unconventional reservoirs is complicated due to the presence of microfractures and multi-scale pores. Multiple methods need to be combined to accurately capture the pore structure of unconventional reservoirs. The combination of experiments and numerical approaches is preferred to accurately monitor fluid transport and distribution during CO_2 flooding to better understand the microscopic flow mechanism in porous media.

(5) The phase behavior of CO_2 and oil is significant for CO_2 flooding performance, and miscible flooding can be achieved between CO_2 and oil under minimum miscible pressure to improve displacement efficiency. However, the mass transfer and phase behavior are rarely considered in microscopic flow models. Therefore, the combination of phase behavior and microscopic flow models at pore-scale need to be investigated and discussed in future work.

Conflicts of Interest

The authors declare that there is no conflict of interest.

Acknowledgement

This work was supported by the National Natural Science Foundation of China (51974268), Key project of Sichuan Science and Technology Department (2019YJ0423), and the Program for Innovative Research Team of the Education Department of Sichuan Province, China (16TD0010).

Nomenclature

C = the BET constant

C_0 = surface tension at gas boiling point, N/m

c_i = the discrete lattice velocity

c_s = a constant associated with the dimensions of space, m/s

e_i = the component of the macro velocity in the discrete direction

E_1 = the adsorption heat of the first layer

E_L = the adsorption heat of each layer

$f_i(x,t)$ = the density distribution function at x space position and i velocity direction at time t

$f_i^{eq}(x,t)$ = the equilibrium density distribution function

F_r = the dimensionless pore shape factor

m_i = the mass of particle i, g/mol

P = the equilibrium pressure, MPa

P_c = the capillary pressure, MPa

P_0 = the saturated steam pressure of adsorbate, MPa

r = pore radius, μm

r_i = the position vector of particle i

r_{ij} = the relative position between particle i and j

R = the gas constant, J/(K·mol)

R_h = the molar heat capacity, J/(K·mol)

S = the pore surface, μm^2

t = the time, ps

T = the experimental temperature, K

T_b = the boiling temperature of gas, K

T_2 = the transverse relaxation time, ms

T_{2B} = the bulk relaxation time, ms

T_{2D} = the diffusion-induced relaxation time, ms

T_{2S} = the surface relaxation time, ms

u = the macro velocity, m/s

V = the pore volume, μm^3

V_e = the equilibrium gas adsorption capacity, cm^3/g

V_m = molar volume of gas, L/mol

V_{ms} = the monolayer saturation adsorption capacity, cm^3/g

$V(r_{ij})$ = the interaction potential function of particle i and j

ρ_c = the conversion coefficient corresponding to each T_2 value, μm/s

ρ = the macro density, g/cm^3

τ = the dimensionless relaxation time, ms

σ = the surface tension, N/m

θ = the contact angle, °

ω_i = the coefficient related to the length of a vector in the direction of discrete velocity

References

[1] O. Hoegh-Guldberg, J. F. Bruno, The impact of climate change on the world’s marine ecosystems. *Science* **2010**, *328* (5985), 1523-1528.

[2] A. A. Lacis, G. A. Schmidt, D. Rind, R. A. Ruedy, Atmospheric CO_2: Principal control knob governing Earth’s temperature. *Science* **2010**, *330* (6002), 356-359.

[3] J. C. Zachos, G. R. Dickens, R. E. Zeebe, An early Cenozoic perspective on greenhouse warming and carbon-cycle dynamics. *Nature* **2008**, *451* (7176), 279-283.

[4] D. P. Schrag, J. A. Higgins, F. A. Macdonald, D. T. Johnston, Authigenic Carbonate and the History of the Global Carbon Cycle. *Science* **2013**, *339* (6119), 540-543.

[5] H. Tian, C. Lu, P. Ciais, A. M. Michalak, J. G. Canadell, E. Saikawa, D. N. Huntzinger, K. R. Gurney, S. Sitch, B. W. Zhang, The terrestrial biosphere as a net source of greenhouse gases to the atmosphere. *Nature* **2016**, *531* (7593), 225-228.

[6] J. Rogelj, M. Den Elzen, N. Höhne, T. Fransen, H. Fekete, H. winkler, R. Schaeffer, F. Sha, K. Riahi, M. Meinshausen, Paris Agreement climate proposals need a boost to keep warming well below 2 C. *Nature* **2016**, *534* (7609), 631-639.

[7] X. Zhou, J. Zhang, J. Li, Industrial structural transformation and carbon dioxide emissions in China. *Energy Policy* **2013**, *57*, 43-51.

[8] M. Bui, C. S. Adjiman, A. Bardow, E. J. Anthony, S. Brown, et al., Carbon capture and storage (CCS): the way forward. *Energy Environ. Sci.* **2018**, *11* (5), 1062-1176.

[9] X. Hao, X. Liao, W. Wang, Z. Rui, The CO_2 storage capacity evaluation: Methodology and determination of key factors, *J. Energy Inst.* **2014** ,*87* (4),pp297-305

[10] Smit, B, Carbon Capture and Storage: introductory lecture. *Faraday Discuss.* **2016**, *192*, 9-25.

[11] G. Cui, Y. Yang, Z. Rui, B. Chen, S. Ren, L Zhang, Assessing the combined influence of fluid-rock interactions on reservoir properties and injectivity during CO_2 storage in saline aquifers, *Energy* **2018**, *155*, 281-296.

[12] Y. Tang, S. Hu, Y. He, et al., Experiment on CO_2-brine-rock interaction during CO_2 injection and storage in gas reservoirs with aquifer. *Chem. Eng. J.* **2020** (review in process).

[13] J. F. Tapia, J. Lee, R. E. Ooi, D. C. Foo, R. R. Tan, A review of optimization and decision-making models for the planning of CO_2 capture, utilization and storage (CCUS) systems. *Sust. Prod. Consump.* **2018**, *13*, 1-15.

[14] L. Li, N. Zhao, W. Wei, Y. Sun, A review of research progress on CO_2 capture, storage, and utilization in Chinese Academy of Sciences. *Fuel* **2013**, *108*, 112-130.

[15] A. Gulzar, A. Gulzar, M. B. Ansari, F. He, S. Gai, P. Yang, Carbon dioxide utilization: A paradigm shift with CO_2 economy. *Chem. Eng. J.A* **2020**, *100013*.

[16] G. Cui, S. Ren, Z. Rui, J. Ezekiel, H. Wang, The influence of complicated fluid-rock interactions on the geothermal exploitation in the CO_2 plume geothermal system, Appl. Energy 2018, *227*, 49-63.

[17] Y. Chen, G. Ma, H. Wang, T. Li, Y. Wang, Z. Sun, Optimizing heat mining strategies in a fractured geothermal reservoir considering fracture deformation effects. *Renew. Energy* **2020**, *148*, 326-337.

[18] Y. Chen, H. Wang, T. Li, Y. Wang, F. Ren, G. Ma, Evaluation of geothermal development considering proppant embedment in hydraulic fractures. *Renew. Energy* **2020**, *153*, 985-997.

[19] X. Zhao, Z. Rui*, X. Liao, R. Zhan, Case studies on the CO_2 storage and EOR in heterogeneous, highly water-saturated, and extra-low permeability Chinese reservoir, *J. Nat. Gas Sci. Eng.* **2015**, *29*, 275-283

[20] Tang, Y., Z. Su, J. He, F. Yang, Numerical Simulation and Optimization of Enhanced Oil Recovery by the In Situ Generated CO_2 Huff-n-Puff Process with Compound Surfactant. *J. Chem.* **2016**, 1-13.

[21] Y. Tang, S. Hu, Y. Wang, L. Ye, Y. Ding, G. Yang, H. Li, Y. Su, Phase behaviors of CO_2 in the whole process of injection–fracturing–flowback: A case study of Well SH52 in a tight sandstone gas reservoir of the Shenmu Gas Field, Ordos Basin. (In Chinese) *Natural Gas Industry* **2019**, *39* (9), 58-64.

[22] Z. Rui, J. Jiang, J. Lu, M. Randy, An integrated technical-economic model for evaluating CO_2 enhanced oil recovery development, *Appl. Energy* **2019**, *247*, 190-211.

[23] X. Zhou, Q. Yuan, Z. Rui, H. Wang, F. Zeng, Feasibility study of CO_2 huff n puff process to enhance heavy oil recovery via long core experiments, *Appl. Energy* **2019**, *236*, 526-539.

[24] Y. He, S. Cheng, Z. Sun, Z. Chai, Z. Rui, Improving Oil Recovery Through Fracture Injection

and Production of Multiple Fractured Horizontal Wells. *J. Energy Resour. Technol.* **2020**, *142* (5): 053002.

[25] R. Iddphonce, J. Wang, L. Zhao, Review of CO_2 injection techniques for enhanced shale gas recovery: prospect and challenges. *J. Nat. Gas Sci. Eng.* **2020**, *77*, 103240.

[26] J. Huang, T. Jin, M. Barrufet, J. Killough, Evaluation of CO_2 injection into shale gas reservoirs considering dispersed distribution of kerogen. *Appl. Energy* **2020**, *260*, 114285.

[27] B. Ren, I. Duncan, Modeling oil saturation evolution in residual oil zones: Implications for CO_2 EOR and sequestration. *J. Pet. Sci. Eng.* **2019**, *177*, 528-539.

[28] B. Ren, I. J. Duncan, Reservoir simulation of carbon storage associated with CO_2 EOR in residual oil zones, San Andres formation of West Texas, Permian Basin, USA. *Energy* **2019**, *167*, 391-401.

[29] L. H. Ribeiro, H. Li, J. E. Bryant, Use of a CO_2-hybrid fracturing design to enhance production from unpropped-fracture networks. *SPE Production & Operations* **2017**, *32* (01), 28-40.

[30] A. Gulzar, A. Gulzar, M. B. Ansari, F. He, S. Gai, P. Yang. Carbon dioxide utilization: A paradigm shift with CO_2 economy. *Chem. Eng. J. A.* **2020**, 100013.

[31] P. Y. Hsieh, W. Y. Sean, T. Sato, Y. W. Seo, Mesoscale modeling of exploiting methane hydrate by CO_2 replacement in homogeneous porous media. *Int. J. Heat Mass Transf.* **2020**, *158*, 119741.

[32] J. Lai, G. Wang, Z. Wang, J. Chen, X. Fan, A review on pore structure characterization in tight sandstones. *Earth-Sci. Rev.* **2018**, *177*, 436-457.

[33] B. Smit, Carbon Capture and Storage: introductory lecture. *Faraday Discuss.* **2016**, *192*, 9-25.

[34] E. Aliakbardoust, H. Rahimpour-Bonab, Effects of pore geometry and rock properties on water saturation of a carbonate reservoir. *J. Pet. Sci. Eng.* **2013**, *112* (Complete), 296-309.

[35] C. R. Clarkson, J. L. Jensen, S. Chipperfield, Unconventional gas reservoir evaluation: what do we have to consider?. *J. Nat. Gas Sci. Eng.* **2012**, *8*, 9-33.

[36] G. Hui, A. O., Wei, X. I. E., Jianpeng, Y. A. N. G., Chuang, Z., Wei, S. (). Pore throat characteristics of extra-ultra low permeability sandstone reservoir based on constant-rate mercury penetration technique.(In Chinese) *Petrol. Geol. Exp.* **2011**, *33* (2), 206-211.

[37] H. Gao, H. Li, Determination of movable fluid percentage and movable fluid porosity in ultra-low permeability sandstone using nuclear magnetic resonance (NMR) technique. *J. Pet. Sci. Eng* **2015**, *133*, 258-267.

[38] C. Zhang, Y. Zhi, R. Zhu, G. Zhang, L. Hou, S. Wu, S. Tao, X. Yuan, D. Dong, Y. Wang, L. Wang, J. Huang, S. Wang, Progress in China's unconventional oil & gas exploration and development and theoretical technologies. *Acta. Geol. Sin-Engl* **2015**, *89* (3), 938-971.

[39] E.W. Washburn, The dynamics of capillary flow, *Phys. Rev* **1921**. *17* (3) 273-283

[40] M. Schmitt, C. P. Fernandes, J. A. da Cunha Neto, F. G. Wolf, V. S. dos Santos, Characterization of pore systems in seal rocks using nitrogen gas adsorption combined with

mercury injection capillary pressure techniques. *Mar. Pet. Geol*. **2013**, *39*,138-149.

[41] P. Li, M. Zheng, H. Bi, S. Wu, X. Wang, Pore throat structure and fractal characteristics of tight oil sandstone: a case study in the Ordos basin, China. *J. Pet. Sci.Eng*. **2017**, *149*, 665-674

[42] J. Jiang, W. Yang, Y. Cheng, K. Zhao, S. Zheng, Pore structure characterization f coal particles via MIP, N_2 and CO_2 adsorption: Effect of coalification on nanopores evolution. *Powder Technol*. **2019**, *354*, 136-148.

[43] H. Gao, W. Xie, J. Yang, C. Zhang, W. Sun, Pore throat characteristics of extraultra low permeability sandstone reservoir based on constant rate mercury penetration technique. *Petro. Geol. Exp*. **2011**, *33* (2), 206-211

[44] X. Li, Y. Kang, M. Haghighi, Investigation of pore size distributions of coals with different structures by nuclear magnetic resonance (NMR) and mercury intrusion porosimetry (MIP). *Measurement* **2018**, *116*, 122-128.

[45] J. Lai, G. Wang, J. Cao, C. Xiao, S. Wang, X Pang, Z. Qin, Investigation of pore structure and petrophysical property in tight sandstones. *Mar. Pet. Geol*. **2018**, *91*, 179-189.

[46] X. Shao, X. Pang, F. Jiang, L. Li, Y. Huyan, D. Zheng, Reservoir characterization of tight sandstones using NMR and IPMI experiments: implication for tight sand gas reservoir quality. *Energy Fuel* **2017**, 31, 10420-10431.

[47] G.R. Coates, R.C.A. Peveraro, A. Hardwick, D. Roberts, **1991**. The magnetic resonance imaging log characterized by comparison with petrophysical properties and laboratory core data. Proceedings of the 66th Annual Technical Conference and Exhibition, Formation Evaluation and Reservoir Geology, *SPE 22723*. pp. 627-635.

[48] R.L. Kleinberg, W.E. Kenyon, P.P. Mitra, Mechanism of NMR relaxation of fluids in rock. *J. Magn. Reson. Ser. A* **1994**, *108* (2), 206-214.

[49] P. Zhang, S. Lu, J. Li, C. Chen, H. Xue, J. Zhang, Petrophysical characterization of oil-bearing shales by low-field nuclear magnetic resonance (NMR). *Mar. Pet. Geol*. **2018** *89*, 775-785.

[50] A. Dillinger, L. Esteban, Experimental evaluation of reservoir quality in Mesozoic formations of the Perth Basin (Western Australia) by using a laboratory low field nuclear magnetic resonance. *Mar. Pet. Geol*. **2014**, *57*, 455-469.

[51] L. Chi, K. Cheng, Z. Heidari, Improved assessment of interconnected porosity in multiple-porosity rocks by use of nanoparticle contrast agents and nuclear-magnetic resonance relaxation measurements. *SPE Reserv. Eval. Eng*. **2016**, 95-107.

[52] H. Daigle, A. Johnson, Combining mercury intrusion and nuclear magnetic resonance measurements using percolation theory. Transp. *Porous Media* **2016**, *111*, 669-679.

[53] E. Müller-Huber, J. Schön, F. Börner, Pore space characterization in carbonate rocks-approach to combine nuclear magnetic resonance and elastic wave velocity measurements. *J. Appl. Geophys*. **2016**, *127*, 68-81.

[54] C. Feng, J. Fu, Y. Shi, G. Li, Z. Mao, Predicting reservoir wettability via well logs. *J. Geophys. Eng*. **2016**, *13* (3), 234-241.

[55] J. Lai, G. Wang, Z. Fan, Z. Zhou, J. Chen, S. Wang, Fractal analysis of tight shaly sandstones using nuclear magnetic resonance measurements. *AAPG Bull*. **2018**, 102 (2), 175-193.

[56] P. Zhao, Z. Wang, Z. Sun, J. Cai, L. Wang, Investigation on the pore structure and multifractal characteristics of tight oil reservoirs using NMR measurements: Permian Lucaogou formation in Jimusaer sag, Junggar Basin. *Mar. Pet. Geol*. **2017**, *86*,1067-1081

[57] H. Gao, H. Li, Determination of movable fluid percentage and movable fluid porosity in ultra-low permeability sandstone using nuclear magnetic resonance (NMR) technique. *J. Pet. Sci. Eng*. **2015**, *133*, 258-267.

[58] I. Langmuir, The constitution and fundamental properties of solids and liquids. Part I. Solids. J. Am. Chem. Soc. **1916**, *38* (11), 2221-2295.

[59] S. Brunauer, P. H. Emmett, E. Teller, Adsorption of gases in multimolecular layers. *J. Am. Chem. Soc.* **1938**, *60*: 309.

[60] S. Chen, S. Tao, D. Tang, H. Xu, S. Li, J. Zhao, H. Yang, Pore structure characterization of different rank coals using N_2 and CO_2 adsorption and its effect on CH4 adsorption capacity: a case in Panguan syncline, western Guizhou, China. *Energy & Fuels* **2017**, *31* (6), 6034-6044.

[61] S. J. Gregg, K. S. W. Sing, H. W. Salzberg, Adsorption Surface Area and Porosity. *J. Electrochem. Soc.* **1967**, *114* (11), 279C.

[62] T. Cao, Z. Song, S. Wang, J. Xia, Characterization of pore structure and fractal dimension of Paleozoic shales from the northeastern Sichuan basin, China. *J. Nat. Gas Sci. Eng*. **2016**, *35*, 882-895.

[63] U. Kuila, M. Prasad, Specific surface area and pore-size distribution in clays and shales. *Geophys. Prospect*. **2013**, *61* (2), 341-362.

[64] Q. Gou, S. Xu, F. Hao, Y. Feng, B. Zhang, Z. Shu, A. Zhang, Y. Wang, X. Cheng, J. Qing, M. Gao, Full-scale pores and micro-fractures characterization using FE-SEM, gas adsorption, nano-CT and micro-CT: A case study of the Silurian Longmaxi Formation shale in the Fuling area, Sichuan Basin, China. *Fuel* **2019**, *253*, 167-179.

[65] Y. Liu, H. A. Li, Y. Tian, Z. Jin, H. Deng. Determination of the absolute adsorption/desorption isotherms of CH_4 and n-C_4H_{10} on shale from a nano-scale perspective. *Fuel*, **2018**, 218, 67-77.

[66] Y. Liu, Z. Jin, H. A. Li. Comparison of Peng-Robinson equation of state with capillary pressure model with engineering density-functional theory in describing the phase behavior of confined hydrocarbons. *SPE Journal*, **2018**, 23, 1, 784-797.

[67] Y. Liu, J. Hou, C. Wang. Absolute adsorption of CH_4 on shale with the simplified local-density theory. *SPE Journal*, 2020.

[68] P. Asmussen, O. Conrad, A. Guenther, M. Kirsch, U. Riller, Semi-automatic segmentation of petrographic thin section images using a "seeded-region growing algorithm" with an

application to characterize weathered subarkose sandstone. *Comput. Geosci*. **2015**, 83, 89-99.

[69] J.C. Eijkel, A. van den Berg, Nanofluidics and the chemical potential applied to solvent and solute transport. *Chem. Soc. Rev* **2010**. *39* (3), 957-973

[70] L. Seungmin, L. Han-Seung, K. Shiho, Pore structure refinement of cement paste incorporating nanosilica: study with dual beam scanning electron microscopy/focused ion beam (SEM/FIB). *Mater. Charact.* **2018**, *145*, 323-328.

[71] M. M. Raith, P. R. Raase, J. R. Reinhardt, Guide to thin section microscopy. **2011**, *University of Bonn*.

[72] R. Richa, T. Mukerji, Y. Keehm, G. Mavko, Image Analysis and Pattern Recognition for Porosity Estimation from Thin Sections. **2006**, *SEG Annual Meeting, New Orleans*.

[73] J. A. Harrell, K. A. Eriksson, Empirical conversion equations for thin-section and sieve derived size distribution parameters. *J. Sediment. Res.* **1979**, *49* (1), 273-280.

[74] A. SchaFer, T. Teyssen, Size, shape and orientation of grains in sands and sandstones-image analysis applied to rock thin-sections. *Sediment. Geol.* **1987**, 52 (3-4), 251-271.

[75] Y. Zhang, H. Zhong, X. Zhang, S. Gao, D. Zhang, Orthogonal microscopy image acq uisition analysis technique for rock sections in polarizer angle domain. *J. Struct. Geol.* **2020**, 104174.

[76] B. Paredis, G. J. Weltje, W. A. Heins, Quantitative analysis of the joint variability of rock texture and composition in thin section: The Generalized Griffiths Descriptor and its application to sediment generation from granitoids. *Earth-Sci. Rev.* **2020**, 103188.

[77] J. Lai, G. Wang. Fractal analysis of tight gas sandstones using high-pressure mercury intrusion techniques. *J. Nat. Gas Sci. Eng.* **2015**, *24*, 185-196.

[78] J. Lai, X. Fan, B. Liu, X. Pang, S. Zhu, W. Xie, Qualitative and quantitative prediction of diagenetic facies via well logs. *Mar. Pet. Geol.* **2020**, *120*, 104486

[79] P. Zhu, Y. Dong, M. Chen, Z. Li, B. Han, J. Wang, Y. Cui, Quantitative evaluation of pore structure from mineralogical and diagenetic information extracted from well logs in tight sandstone reservoirs. *J. Nat. Gas Sci. Eng.* **2020**, *80*, 103376.

[80] D. Xiao, Z. Lu, S. Jiang, S. Lu, Comparison and integration of experimental methods to characterize the full-range pore features of tight gas sandstone-a case study in Songliao basin of China. *J. Nat. Gas Sci. Eng* **2016**, *34*, 1412-1421.

[81] H. Li, H. Li, B. Gao, W. Wang, C. Liu, Study on pore characteristics and microstructure of sandstones with different grain sizes. *J. Appl. Geophys.* **2017**, *136*, 364-371.

[82] A. Bellissimo, G. M. Pierantozzi, A. Ruocco, G. Stefani, O. Y. Ridzel, V. Astasausksas , W. S. M. Werner, M. Taborelli. Secondary electron generation mechanisms in carbon allotropes at low impact electron energies. *J. Electron Spectrosc. Relat. Phenom.* **2020**, *241*, 146883.

[83] S. Zhou, D. Liu, Y. Cai, Y. Yao, Z. Li, 3D characterization and quantitative evaluation of pore-fracture networks of two Chinese coals using FIB-SEM tomography. *Int. J. Coal Geol.* **2017**, 174, 41-54.

[84] Y. Song, C. A. Davy, D. Troadec, X. Bourbon, Pore network of cement hydrates in a high performance concrete by 3D FIB/SEM-implications for macroscopic fluid transport. *Cem. Concr. Res.* **2019**, *115*, 308-326.

[85] A. C. G. Fonseca, L. F. Costa, C. C. Dantas, R. J. S. B. Heck, Melo, A. C. D. Antonino, E. S. Barbosa, Precise determination of soil structure parameters in a X-ray and γ-ray CT combination methodology. *Prog. Nucl. Energy* **2019**, *114*, 138-144.

[86] H. Villarraga-Gómez, E. L. Herazo, S. T. Smith, X-ray computed tomography: from medical imaging to dimensional metrology. *Precis. Eng.* **2019**, *60*, 544-569.

[87] A. Scanziani, K. Singh, H. Menke, B. Bijeljic, M. J. Blunt, Dynamics of enhanced gas trapping applied to CO_2 storage in the presence of oil using synchrotron X-ray micro tomography. *Appl. Energy* **2020**, *259*, 114136.

[88] M. J. Blunt, B. Bijeljic, H. Dong, O. Gharbi, S. Iglauer, P. Mostaghimi, A. Paluszny, C. Pentland, Pore-scale imaging and modelling. *Adv. Water Resour.* **2013**, 51, 197-216.

[89] D. P. Lymberopoulos, A. C. Payatakes, Derivation of topological, geometrical, and correlational properties of porous media from pore-chart analysis of serial section data. *J. Colloid Interface Sci.* **1992**, *150* (1):61-80.

[90] H. J. Vogel, K. Roth, Quantitative morphology and network representation of soil pore structure. *Adv. Water Resour.* **2001**, *24* (3-4): 233-242.

[91] J. T. Fredrich, B. Menendez, T. F. Wong, Imaging the pore structure of geomaterials. *Science* **1995**, *268* (5208), 276-279.

[92] B. G. Chae, Y. Ichikawa, G. C. Jeong, Y. S. Seo, B. C. Kim, Roughness measurement of rock discontinuities using a confocal laser scanning microscope and the Fourier spectral analysis. *Eng. Geol.* **2004**, *72* (3-4), 181-199.

[93] N. Saxena, R. Hofmann, F. O. Alpak, S. Berg, J. Dietderich, U. Agarwal, K. Tandon, S. Hunter, J. Freeman, O. B. Wilson, References and benchmarks for pore-scale flow simulated using micro-CT images of porous media and digital rocks. *Adv. Water Resour* **2017**, *109*, 211-235.

[94] L. Kong, M. Ostadhassan, X. Hou, M. Mann, C. Li, Microstructure characteristics and fractal analysis of 3D-printed sandstone using micro-CT and SEM-EDS. *J. Pet. Sci. Eng.* **2019**, *175*, 1039-1048.

[95] W. Lv, S. Chen, Y. Gao, C. Kong, N. Jia, L. He, W. Rong, J. Li, Evaluating seepage radius of tight oil reservoir using digital core modeling approach. *J. Pet. Sci. Eng* **2019**, *178*, 609-615.

[96] M. Ioannidis, M. Kwiecien, I. Chatzis, Computer generation and application of 3-D model porous media: from pore-level geostatistics to the estimation of formation factor. *In Petroleum Computer Conference*, **1995** January. Society of Petroleum Engineers.

[97] S. Bekri, K. Xu, F. Yousefian, P. M. Adler, J. F. Thovert, Pore geometry and transport properties in North Sea chalk. *J. Pet. Sci. Eng.* **2000**, *25* (3-4), 107-134.

[98] R. D. Hazlett, Statistical characterization and stochastic modeling of pore networks in relation

to fluid flow. *Math. geol.* **1997**, *29* (6), 801-822.

[99] I. Hidajat, A. Rastogi, M. Singh, K. K. Mohanty, Transport properties of porous media reconstructed from thin-sections. *SPE Journal* **2002**, *7* (01), 40-48.

[100] P. E. Oren, S. Bakke, O. J. Arntzen, Extending predictive capabilities to network models. *SPE journal* **1998**, *3* (04), 324-336.

[101] M. Pilotti, Reconstruction of clastic porous media. *Transp. Porous Media* **2000**, *41* (3), 359-364.

[102] S. An, J. Yao, Y. Yang, L. Zhang, J Zhao, Y. Gao, Influence of pore structure parameters on flow characteristics based on a digital rock and the pore network model. *J. Nat. Gas Sci. Eng.* **2016**, *31*, 156-163.

[103] H. Fang, S. Sang, S. Liu, Y. Du, Methodology of three-dimensional visualization and quantitative characterization of nanopores in coal by using FIB-SEM and its application with anthracite in Qinshui basin. *J. Pet. Sci. Eng.* **2019**, *182*, 106285.

[104] Y. Zhang, H. Khorshidian, M. M. Ashani, A. Sanati-Nezhad, S. H. Hejazi, Functionalized Multiscale Visual Models to Unravel Flow and Transport Physics in Porous Structures. *Water Res.* **2020**, 115676.

[105] B. Bao, J. Riordon, F. Mostowfi, D. Sinton, Microfluidic and nanofluidic phase behaviour characterization for industrial CO_2, oil and gas. *Lab Chip* **2017** ,*17* (16), 2740-2759.

[106] A. C. Gunde, B. Bera, S. K. Mitra, Investigation of water and CO_2 (carbon dioxide) flooding using micro-ct (micro-computed tomography) images of berea sandstone core using finite element simulations. *Energy* **2010**, *35* (12), 5209-5216.

[107] M. Khather, A. Saeedi, M. B. Myers, M. Verrall, An experimental study for carbonate reservoirs on the impact of CO_2-EOR on petrophysics and oil recovery. *Fuel* **2019**, *235*, 1019-1038.

[108] F. Du, B. Nojabaei, Estimating diffusion coefficients of shale oil, gas, and condensate with nano-confinement effect. *J. Pet. Sci. Eng.* **2020**, 107362.

[109] L. Wang, Y. He, Q. Wang, M. Liu, X. Jin. Multiphase flow characteristics and EOR mechanism of immiscible CO_2 water-alternating-gas injection after continuous CO_2 injection: A micro-scale visual investigation. *Fuel*, **2020**, 282, 118689.

[110] M. Alfi, D. Banerjee, H. Nasrabadi, Effect of confinement on the dynamic contact angle of hydrocarbons. *Energy Fuels* **2016**, *30* (11), 8962-8967.

[111] Y. Song, C. Zhao, M. Chen, Y. Chi, Y. Zhang, J. Zhao, Pore-scale visualization study on CO_2 displacement of brine in micromodels with circular and square cross sections. *Int. J. Greenh. Gas Control* **2020**, *95*. 102958.

[112] M. Cui, R. Wang, C. Lv, Y. Tang, Research on microscopic oil displacement mechanism of CO_2 EOR in extra-high water cut reservoirs. *J. Pet. Sci. Eng.* **2017**, *154*, 315-321.

[113] K. Xu, T. Liang, P. Zhu, P. Qi, J. Lu, C. Huh, M. Balhoff, A 2.5-D glass micromodel for investigation of multi-phase flow in porous media. *Lab Chip* **2017**, *17* (4), 640–646.

[114] M. Sharifipour, A. Nakhaee, P. Pourafshary, Model development of permeability impairment due to clay swelling in porous media using micromodels. *J. Pet. Sci. Eng.* **2019**, *175*, 728-742.

[115] B. Bai, Y. Zhang, C. Zhou, C. Qu, X. He, Fabrication and verification of a glass-silicon-glass micro-/nanofluidic model for investigating multi-phase flow in shale-like unconventional dual-porosity tight porous media. Lab Chip 2019, 19(24).

[116] L. Mejia, P. Zhu, J. D. Hyman, K. K. Mohanty, M. T. Balhoff, Coreflood on a chip: Core-scale micromodels for subsurface applications. *Fuel* **2020**, *281*, 118716.

[117] D. Albayati, A. Saeedi, M. Myers, C. White, Q. Xie, Insights into immiscible supercritical CO_2 EOR: An XCT scanner assisted flow behaviour in layered sandstone porous media. *J. CO_2 Util.* **2019**, 32, 187-195.

[118] L. Xu, M. Myers, Q. Li, C. White, X. Zhang. Migration and storage characteristics of supercritical CO_2 in anisotropic sandstones with clay interlayers based on X-CT experiments. *J Hydrol*, **2020**, 580, 124239.

[119] D. Du, Y. Li, D. Zhang, X. Dong, F. Wang, K. Chao, Experimental study on the inlet behavior of CO_2 foam three phase displacement processes in porous media. *Exp. Therm. Fluid Sci.* **2019**, *103*, 247-261.

[120] Y. Liu, Y. Teng, G. Lu, L. Jiang, J. Zhao, Y. Zhang, Y. Song, Experimental study on CO_2 diffusion in bulk n-decane and n-decane saturated porous media using micro-CT. *Fluid Phase Equilib.* **2016**, *417*, 212-219.

[121] B. Wei, X. Zhang, R. Wu, P. Zou, K. Gao, X. Xu, W. Pu, C. Wood, Pore-scale monitoring of CO_2 and N_2 flooding processes in a tight formation under reservoir conditions using nuclear magnetic resonance (NMR): A case study. *Fuel* **2019**, *246*, 34-41.

[122] S. Li, Q. Wang, K. Zhang, Z. Li, Monitoring of CO_2 and CO_2 oil-based foam flooding processes in fractured low-permeability cores using nuclear magnetic resonance (NMR). *Fuel* **2020**, *263*, 116648.

[123] D. Du, W. Pu, F. Jin, R. Liu, Experimental Study on EOR by CO_2 Huff-n-Puff and CO_2 Flooding in Tight Conglomerate Reservoirs with Pore Scale. *Chem. Eng. Res. Des.* **2020**, 425-432.

[124] F. Mo, Z. Du, X. Peng, Y. Tang, H. Sun, Pore-scale analysis of flow resistance in tight sandstones and its relationship with permeability jail. *J. Nat. Gas Sci. Eng.* **2017**, *44,* 314-327.

[125] P. Xiao, Z. Yang, X. Wang, H. M. Xiao, X. Wang, Experimental investigation on CO_2 injection in the Daqing extra/ultra-low permeability reservoir. *J. Pet. Sci. Eng.* **2017**, *149*, 765-771.

[126] Y. Zhan, Y. Zhang, X. Lei, Y. Zhang, Y. Song. CO_2 flooding enhanced oil recovery evaluated using magnetic resonance imaging technique. *Energy*, **2020,** 117878.

[127] B. Wei, X. Zhang, R. Wu, P. Zou, K. Gao, X. Xu, W. Pu, C. Wood. Pore-scale monitoring of CO_2 and N_2 flooding processes in a tight formation under reservoir conditions using nuclear

magnetic resonance (NMR): A case study. *Fuel*, **2019**, 246, 34-41.

[128] S. Li, Q. Wang, K. Zhang, Z. Li. Monitoring of CO_2 and CO_2 oil-based foam flooding processes in fractured low-permeability cores using nuclear magnetic resonance (NMR). *Fuel*, **2020**, 263, 116648.

[129] D. Du, W. Pu, F. Jin, R. Liu. Experimental study on EOR by CO_2 huff-n-puff and CO_2 flooding in tight conglomerate reservoirs with pore scale. *Chem. Eng. Res. Des*, **2020**, 425-432.

[130] M. Chen, J. Dai, X. Liu, Y. Kuang, Z. Wang, S. Gou, M. Qin, M. Li. Effect of displacement rates on fluid distributions and dynamics during water flooding in tight oil sandstone cores from nuclear magnetic resonance (NMR). *J. Pet. Sci. Eng*. **2020**, 184, 106588.

[131] J. G. Harris, K. H. Yung, Carbon dioxide's liquid-vapor coexistence curve and critical properties as predicted by a simple molecular model. *J. Phys. Chem.* **1995**, *99* (31), 12021-12024.

[132] J. Yang, Y. Ren, A. M. Tian, H. Sun, COMPASS force field for 14 inorganic molecules, He, Ne, Ar, Kr, Xe, H_2, O_2, N_2, NO, CO, CO_2, NO_2, CS_2, and SO_2, in liquid phases. *J. Phys. Chem. B* **2000**, *104* (20), 4951-4957.

[133] J. J. Potoff, J. I. Siepmann, Vapor-liquid equilibria of mixtures containing alkanes, carbon dioxide, and nitrogen. *AICHE J.* **2001**, 47 (7), 1676-1682.

[134] D. Beeman, Some multistep methods for use in molecular dynamics calculations. *J. Comput. Phys.* **1976**, *20* (2), 130-139.

[135] C. W. Gear, Numerical initial value problems in ordinary differential equations. *Math. Comput.* **1973**, *27* (123), 673.

[136] R. W. Hockney, The potential calculation and some applications. *Methods Comput. Phys.* **1970**, *9*, 136.

[137] M. Seyyedattar, S. Zendehboudi, S. Butt, Molecular dynamics simulations in reservoir analysis of offshore petroleum reserves: A systematic review of theory and applications. *Earth-Sci. Rev.* **2019**, *192*, 194-213.

[138] J. Meller, **2001**. Molecular Dynamics: Encyclopedia of Life Sciences.

[139] H. Czichos, T. Saito, **2006**. Springer handbook of materials measurement methods (Vol. 978). L. Smith (Ed.). Berlin: Springer.

[140] T. Fang, M. Wang, C. Wang, B. Liu, Y. Shen, C. Dai, J. Zhang, Oil detachment mechanism in CO_2 flooding from silica surface: Molecular dynamics simulation. *Chem. Eng. Sci.* **2017**, *164*, 17-22.

[141] R. Wang, F. Peng, K. Song, G. Feng, Z. Guo, Molecular dynamics study of interfacial properties in CO_2 enhanced oil recovery. *Fluid Phase Equilib.* **2018**, *467*, 25-32.

[142] T. Fang, M. Wang, Y. Gao, Y. Zhang, Y. Yan, J. Zhang, Enhanced oil recovery with CO_2/N_2 slug in low permeability reservoir: Molecular dynamics simulation. *Chem. Eng. Sci.* **2019**, *197*, 204-211.

[143] X. Li, S. Wang, Q. Feng, Q. Xue, The miscible behaviors of $C_{10}H_{22}$ ($C_7H_{17}N$)/C_3H_8 system: Insights from molecular dynamics simulations. *Fuel* **2020**, *279*, 118445.

[144] A. J. C. Ladd, R. Verberg, Lattice-boltzmann simulations of particle-fluid suspensions. *J. Stat. Phys.* **2001**, *104* (5-6), 1191-1251.

[145] R. R. Nourgaliev, T. N. Dinh, T. G. Theofanous, D. Joseph, The lattice Boltzmann equation method: theoretical interpretation, numerics and implications. *Int. J. Multiph. Flow* **2003**, *29* (1), 117-169.

[146] J. Huang, X. Yin, J. Killough, Thermodynamic consistency of a pseudopotential lattice Boltzmann fluid with interface curvature. *Phys. Rev. E* **2019**, *100* (5), 053304.

[147] D. Raabe, Overview of the lattice Boltzmann method for nano-and microscale fluid dynamics in materials science and engineering. *Model. Simul. Mater. Sci. Eng.* **2004**, *12* (6), R13.

[148] H. Huang, M. Sukop, X. Lu, Multiphase lattice Boltzmann methods: Theory and application. *John Wiley & Sons*. **2015**

[149] Q. Li, K. H. Luo, Q. J. Kang, Y. L. He, Q. Chen, Q. Liu, Lattice boltzmann methods for multiphase flow and phase-change heat transfer. *Prog. Energy Combust. Sci.* **2016**, *52,* 62-105.

[150] S. Bakhshian, S. A. Hosseini, Pore-scale analysis of supercritical CO_2-brine immiscible displacement under fractional-wettability conditions. *Adv. Water Resour.* **2019**, *126*, 96-107.

[151] T. Zhao, H. Zhao, X. Li, Z. Ning, Q. Wang, W. Zhao, J. Zhang, Pore scale characteristics of gas flow in shale matrix determined by the regularized lattice Boltzmann method. *Chem. Eng. Sci.* **2018**, *187*, 245-255.

[152] H. Liu, A. J. Valocchi, C. Werth, Q. Kang, M. Oostrom, Pore-scale simulation of liquid CO_2 displacement of water using a two-phase lattice Boltzmann model. *Adv. Water Resour* **2014**, *73*, 144-158.

[153] J. Hardy, O. De Pazzis, Y. Pomeau, Molecular dynamics of a classical lattice gas: transport properties and time correlation functions. Phys. Rev. A **1976**, *13* (5), 1949-1961.

[154] Broadwell, E. James, Shock structure in a simple discrete velocity gas. *Phys. Fluids* 1964, *7* (8), 1243.

[155] Z. Guo, B. Shi, N. Wang, Lattice BGK model for incompressible Navier-Stokes equation. *J. Comput. Phys.* **2000**, *165* (1), 288-306.

[156] Y. H. Qian, D. d'Humières, P. Lallemand, Lattice BGK models for Navier-Stokes equation. *EPL* (*Europhysics Letters*) **1992**, *17* (6), 479.